

¹ Topographic Effects on Internal Waves at
² Barkley Canyon

³ Kurtis Anstey
⁴ V00939802
⁵ Department of Physics and Astronomy
⁶ University of Victoria
⁷ May 20, 2022

⁸ Dr. Jody Klymak (University of Victoria)
⁹ Dr. Steven Mihaly (Ocean Networks Canada)
¹⁰ Dr. Richard Thomson (Institute of Ocean Sciences)

11 Table of Contents

12	List of Figures	3
13	1 Abstract	4
14	2 Introduction	5
15	3 Internal wave theory	8
16	4 Site and methods	13
17	5 Results	19
18	5.1 Observations	19
19	5.1.1 Mean currents	19
20	5.1.2 High-passed currents	20
21	5.1.3 Depth dependence	23
22	5.2 Band-integrated depth and seasonal changes	25
23	5.2.1 Sub-diurnal	25
24	5.2.2 Diurnal	27
25	5.2.3 Near-inertial	30
26	5.2.4 Semidiurnal	34
27	5.2.5 High-frequency internal wave continuum	37
28	5.2.6 Near- N	43
29	6 Discussion	46
30	6.1 Canyon axis mean currents	46
31	6.2 Tidal currents	48
32	6.3 Near-inertial forcing	50
33	6.4 Continuum-dissipation estimates	52
34	6.5 Near- N spectral shoulder energy	53
35	7 Summary and conclusions	55
36	8 References	57
37	A Appendix: Supplemental plots	64
38	A.1 Wind comparisons	64

39 List of Figures

40 1	Internal wave processes	6
41 2	Internal waves in a two-layer system	7
42 3	Internal waves and topography	8
43 4	Barkley Canyon site map and semidiurnal criticality	10
44 5	Site topography	11
45 6	Radiating internal waves in a lab	12
46 7	ADCP frequency, instrument ID, deployment, and data availability	13
47 8	QC threshold profiles	14
48 9	Mean stratification and WKB scaling factor	16
49 10	Low-pass velocities	18
50 11	AXIS along-canyon mean-flow	19
51 12	High-pass velocities - April 2013	20
52 13	PSD and rotary spectra	21
53 14	Depth-frequency PSD	24
54 15	Depth-band PSD - Sub-diurnal	26
55 16	Depth-band PSD - Diurnal	28
56 17	Diurnal spring-neap forcing	29
57 18	Depth-band rotary PSD - Near-inertial	31
58 19	Near-inertial vertical energy propagation	32
59 20	Near-inertial delayed deep response histogram	32
60 21	Near-inertial slab response - 2013	33
61 22	Depth-band PSD - Semidiurnal	35
62 23	Semidiurnal spring-neap forcing	36
63 24	Depth-band PSD - Continuum	38
64 25	Continuum power law fits	39
65 26	Dissipation and diffusivity	40
66 27	Dissipation univariate power law fits	41
67 28	Dissipation multivariate power law fits	43
68 29	Depth-band PSD - Near- N shoulder	44
69 30	Shoulder-dissipation power law fits	45
70 31	High frequency-resolution PSD - 2013	51
71 32	Appendix A - Near-inertial wind comparisons - 2014	64
72 33	Appendix A - Near-inertial wind comparisons - 2017	65
73 34	Appendix A - Near-inertial wind comparisons - 2018	66

74 1 Abstract

75 Submarine canyons incising the continental shelf and slope are hot spots for
76 topography-internal wave interactions, with elevated dissipation and mixing
77 contributing to regional transport and biological productivity. At two Barkley
78 Canyon sites (the continental slope below the shelf-break, and deep within the
79 canyon), four overlapping years of horizontal velocity time-series data are used
80 to examine the effects of irregular topography on the internal wave field. Mean
81 currents are topographically guided at both sites, and in the canyon there is an
82 inter-annually consistent, periodic (\sim week) up-canyon flow (-700 to -900 m)
83 above a near-bottom down-canyon layer. There is elevation of internal wave
84 energy near topography, up to a factor of 10, 130 m above the slope, and up to
85 a factor of 100, 230 m above the canyon bottom. All bands display weak inter-
86 annual variability, but significant seasonality. Sub-diurnal and diurnal flows
87 are presumably sub-inertially trapped along topography, and the diurnal band
88 appears to be forced locally (barotropically). Both sites have high near-inertial
89 energy. At the slope site, near-inertial energy is attenuated with depth, while
90 in the canyon it is amplified near the bottom. Both sites show intermittent
91 near-inertial forcing associated with wind events, downward propagation of
92 high-mode internal waves, and the seasonal mixed-layer depth, though fewer
93 events are observed in the canyon. Free semidiurnal internal tides are focused
94 and reflected near critical shelf-break and canyon floor topography, and appear
95 to experience both local and remote (baroclinic) forcing. The high-frequency
96 internal wave continuum has enhanced energy near bottom at both sites (up
97 to $7\times$ the open-ocean Garrett-Munk spectrum), and inferred dissipation rates,
98 ϵ , increasing from a background of less than 10^{-9} W kg $^{-1}$ and reaching 10^{-7}
99 W kg $^{-1}$ near topography. Dissipation is most strongly correlated with the
100 semidiurnal (M_2) constituent at both sites, with secondary contributions from
101 the sub-diurnal (Sub_{K_1}) band on the slope, and the NI band in the canyon.
102 Power laws for these dependencies are $\epsilon \sim M_2^{0.83} + \text{Sub}_{K_1}^{0.59}$ at the slope, and
103 $\epsilon \sim M_2^{1.47} + \text{NI}^{0.24}$ in the canyon. There is evidence in spectra of a near- N
104 build-up of energy correlated with high-frequency continuum variability, with
105 a power law fit of $P_{Sh} \sim \epsilon^{0.34 \pm 0.08}$ that is independent of site topography.
106 Though some general results are expected from observations at other slope
107 and canyon sites, the greater temporal extent of these data provide a uniquely
108 long-term evaluation of such processes.

109 2 Introduction

110 Internal waves (IW) are slow-moving, low-frequency, sub-surface gravity waves
111 that exist within density gradients in the ocean interior (Garrett & Munk,
112 1979). They have horizontal wavelengths up to kilometres long, and oscillate
113 in a range between the local Coriolis (inertial, f) and Brunt–Väisälä (buoy-
114 ancy, N) frequencies (Garrett & Munk, 1979). They are forced by weather -
115 as near-inertial (NI) IW generated by surface winds exciting currents in the
116 mixed layer (ML) that pump energy into the interior (Garratt, 1977) - or
117 by tides and currents moving across irregular seafloor topography, generating
118 baroclinic internal tides (IT) and IW that can propagate through the stratified
119 ocean (Hendershott & Garrett, 2018). As travelling IW approach irregular to-
120 pography, such as continental slopes or submarine canyons, they can focus and
121 break, leading to elevated mixing. As mixing can be linked to ocean circula-
122 tion, biogeochemical cycles, weather, and long-term climate (Kunze, 2017), it
123 is important to understand forcing by the IW field. As incident IW and IT
124 have varying origins, amplitudes, and frequencies, each responds differently
125 to the influence of impacted topography. Sub-inertial IW and IT may be
126 trapped along topography, while those that are NI or super-inertial are free
127 to reflect and propagate through open water. By characterising the IW and
128 IT that comprise the local IW field, it may be possible to better quantify and
129 understand IW driven turbulence and mixing.

130 As the wind, currents, and tides are ever-present, IW are prevalent ocean phe-
131 nomena. As early as the mid-19th century, notable scientists such as Stokes
132 and Rayleigh were investigating properties of fluid density and stratification,
133 essential for IW propagation (Garrett & Munk, 1979). IW were mistaken
134 as consistent noise in early 20th-century hydrocast readings, and Ekman dis-
135 cussed their effects in his seminal theories on fluid mechanics (Garrett & Munk,
136 1979). In the late-20th century, Garrett and Munk (1979) developed the canon-
137 ical Garrett-Munk (GM) spectrum defining the characteristic frequency and
138 wavenumber continuum of open-ocean IW, to better understand their role in
139 ocean processes. Instrumentation improved, and scientists continued to un-
140 cover the contributions of IW to physical systems of all scales, from fine-scale
141 mixing to the large-scale meridional overturning circulation (Figure 1; Garrett
142 & Munk, 1979). Recently, studies have linked IW generation and dissipation to
143 the global oceanic energy budget (Carter & Gregg, 2002; Kunze et al., 2002;
144 Terker et al., 2014; Kunze, 2017), tide and wind forcing of IW to seasonal
145 variability of regional circulation processes (Alford et al., 2012; Thomson &
146 Krassovski, 2015), and enhanced mixing to IW interactions with irregular to-
147 pography (Nash et al., 2004; Kunze et al., 2012; Gemmrich & Klymak, 2015).

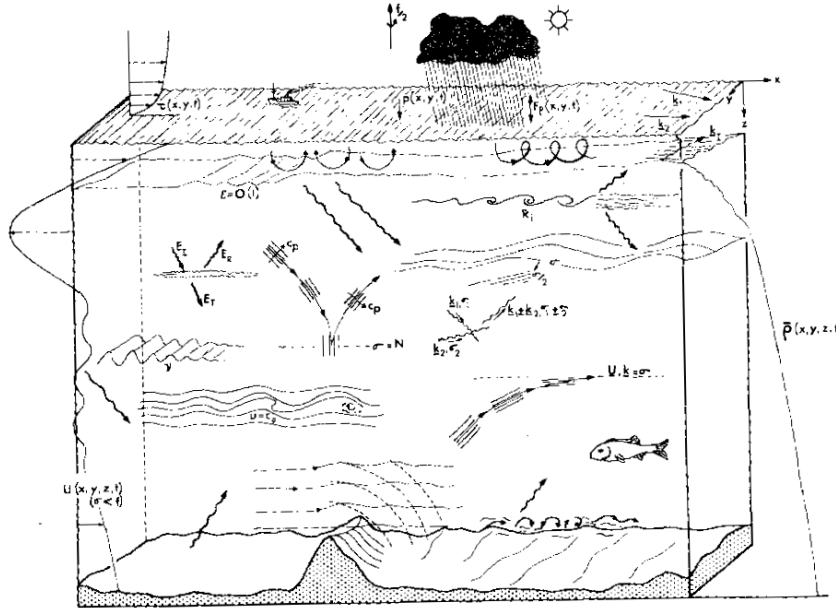


Figure 1. Generalised depiction of IW processes in the ocean, as envisioned by Garrett and Munk (1979). IW are forced by, coincide with, or contribute to most physical processes in the ocean.

- 148 Further research on IW interactions with irregular topography is thought to
 149 be essential to understanding seasonal upwelling, diapycnal mixing, and cross-
 150 shelf exchange (Burrier, 2019). As IW and IT approach seamounts, slopes,
 151 or canyons, nonlinear processes may cause their energy to reflect, scatter,
 152 or focus and break (Figure 3), dissipating as heat (Garrett & Munk, 1979;
 153 Klymak et al., 2006; Kunze et al., 2012). Dissipation leads to an energetic
 154 local environment, evident as near-bottom turbulent processes on the fine- (1
 155 - 100 m vertical) and micro-scales (< 1 m vertical) (Garrett & Munk, 1979;
 156 Carter & Gregg, 2002; Kunze et al., 2002; Kunze et al., 2012). These processes
 157 lead to the elevated mixing of pollutants and biological constituents, and drive
 158 regional transport of energy and momentum (Kunze et al., 2012). Topography-
 159 forced IW mixing helps set ocean stratification, layers that even influence the
 160 large-scale ocean-atmosphere coupled climate system (Garett & Munk, 1979).
- 161 In Canada, IW are regularly observed on the highly productive Vancouver Is-
 162 land Continental Shelf (VICS) (Thomson & Crawford, 1982; Allen et al., 2001),
 163 a relatively broad (about 80 km) shelf region with a canyon-incised continen-
 164 tal slope. Regional observations have led to insight on non-linear wave-wave
 165 interactions between surface generated NI IW and upward propagating semidi-
 166urnal IT (Mihaly et al., 1998), and the presence of diurnal baroclinic shelf
 167 waves forced by tidal oscillations near the mouth of the Juan de Fuca Strait

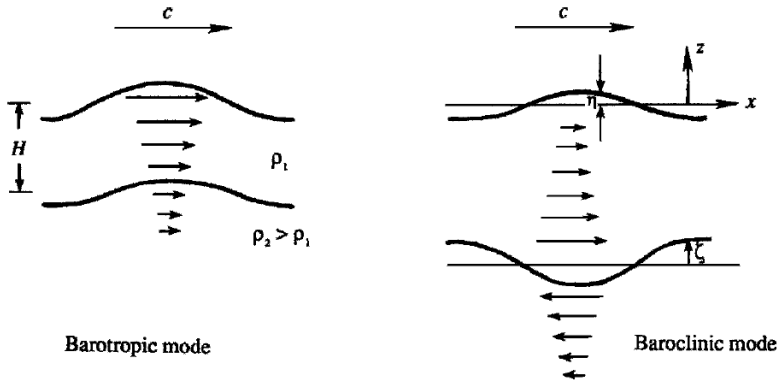


Figure 2. IW in a two-layer system. Graphic representation of the difference between barotropic and baroclinic flows. Adapted from Kundu & Cohen (2008).

(Thomson & Crawford, 1982). Seasonally variable regional currents (Thomson & Krassovski, 2015) have been associated with observations of vorticity stretching and upwelling at the head of shelf-incising Barkley Canyon, suggesting considerable influence by this canyon on VICS water properties, transport of biological constituents, and overall shelf productivity (Allen et al., 2001; Juniper et al., 2013; Doya et al., 2013; Chauvet et al., 2018). However, there is a lack of topography-IW observations at Barkley Canyon necessary to properly characterise its influence on the physical processes of the VICS. Further research into Barkley Canyon's IW field can provide insight into the effects of topography-driven mixing on the productivity of not only the VICS, but global shelf sites adjacent to canyon-incised continental slopes.

This study uses IW theory (Section 3) to evaluate horizontal velocity data from two Barkley Canyon sites (Section 4), one on the adjacent continental slope and one within the canyon, to characterise the topographic interactions of IW and IT, and their potential influence on local mixing. Mean currents (Section 5.1.1), and IW (Section 5.1.2) of sub-tidal, tidal, NI, and super-tidal (high-frequency IW continuum and near- N) frequency bands are evaluated for depth-dependence (Section 5.1.3) and seasonality (Section 5.2), including a forcing analysis of variability due to regional currents, tides, and wind. The high-frequency IW continuum (Section 5.2.5) is further evaluated for topographic influence through comparison with open-ocean GM theory, leading to approximations of dissipation and diffusivity to estimate mixing. The seasonal energy of the high-frequency continuum is correlated to low-frequency constituents to identify which bands contribute most to high-frequency turbulent processes. A near- N build-up of energy (Section 5.2.6) is also evaluated

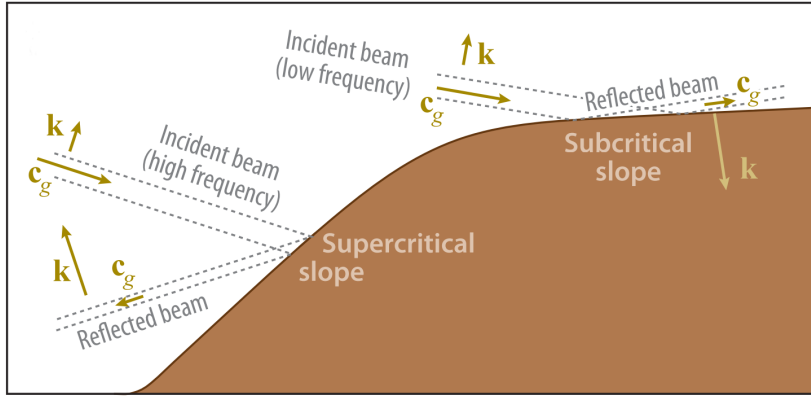


Figure 3. Graphic of IW interactions with slope topography (Lamb, 2014). The propagation angle of an IW depends on frequency and stratification. Depending on the slope of topography, incident IW can be scattered up, reflected down, or focused, possibly breaking.

for variability and energy contributions from lower frequency bands. Key findings include deep-canyon topography-guided mean current layers (Section 6.1), near-topography focusing of tidal energy with frequency-dependent seasonality and forcing (Section 6.2), attenuation of downward NI IW energy above the continental slope (Section 6.3), elevated high-frequency IW continuum energy and dissipation linked to the semidiurnal constituent (Section 6.4), and an energetic near- N band that is seasonally correlated with high-frequency continuum energy (Section 6.5).

3 Internal wave theory

Vertical displacements in a fluid can be classified as either barotropic, where the displacement is dependent only on pressure, $P(z)$ (where z is depth), or as baroclinic, where the displacement is also a function of density, $\rho(z)$, temperature, $T(z)$, etc. (Figure 2). For example, surface tides are barotropic, affecting most of the water column as the surface oscillates, while IW are baroclinic, perturbations that exist along density interfaces in the stratified ocean interior. IW are highly dependent on stratification, characterised by the depth-dependent buoyancy frequency, $N(z)$, defined as:

$$N^2(z) = -\frac{g}{\rho_0} \frac{d\rho}{dz} \quad (1)$$

where g is the acceleration due to gravity, and ρ_0 a constant reference density. In continuously stratified fluids such as the ocean interior, IW may exist both

213 non-isotropically and rotationally, with the relative effects of clockwise (CW)
 214 and counter-clockwise (CCW) rotation described by the consistency relation:

$$215 \quad \frac{CW}{CCW} = \frac{(\omega + f)^2}{(\omega - f)^2} \quad (2)$$

216 where ω is frequency, and f the Coriolis frequency ($f = 2\Omega\sin\phi$, where Ω is the
 217 rotation rate of the Earth, and ϕ is latitude). f and $N(z)$ are the lower and
 218 upper frequency bounds for 'free' IW (Kundu & Cohen, 2008). IW generated
 219 outside this frequency range are evanescent (trapped) to topography, unable
 220 to radiate into the ocean interior (Flather, 1988).

221 As free IW and IT approach irregular topography (continental slopes, sub-
 222 marine canyons, etc.), the angle of the incident wave ray, α , and the slope
 223 of the topography, β , have an influential relationship on the behaviour of the
 224 topography-IW interaction (Figure 3) (Lamb, 2014). The ray path of an inci-
 225 dent, free IW in a continuously stratified fluid is defined as (Nash et al., 2004;
 226 Garrett & Kunze, 2007; Lamb, 2014):

$$227 \quad \alpha(z) = \sqrt{\frac{(\omega^2 - f^2)}{(N(z)^2 - \omega^2)}} \quad (3)$$

228 where α depends on $N(z)$, so the ray path tends to bend with depth. The
 229 impacted bathymetric slope, $\beta = \nabla H$, is determined from the gradient mag-
 230 nitude of the local topography, and compared with α to identify regions where
 231 IW and IT may break or reflect, known as criticality (Martini et al., 2011).
 232 For Barkley Canyon, criticality of the semidiurnal constituent is depicted in
 233 Figure 4. If $\beta > \alpha$, the slope is supercritical and incident wave energy is
 234 reflected downward (see Figure 5). For $\beta \approx \alpha$, the slope is near-critical and
 235 incident wave energy is focused, potentially leading to non-linear breaking and
 236 dissipation. If $\beta < \alpha$, the slope is considered subcritical and incident wave en-
 237 ergy is scattered upward (Klymak et al., 2011; Lamb, 2014). When IW reflect
 238 from critical topography the wave frequency, angles of incidence and reflection,
 239 and energy flux are conserved. However, energy density and wave amplitude
 240 increase, corresponding to decreased wavelengths and group velocity, resulting
 241 in a focused, energetic layer near topography (Thorpe, 2001; Lamb, 2014).

242 Intensified near-slope layers are not uncommon (Polzin et al., 1997; Nash et al.,
 243 2004; Kunze et al., 2012), and can elevate IW energy multiple orders of mag-
 244 nitude with depth-dependent vertical scales hundreds of metres above bottom
 245 (Hotchkiss & Wunsch, 1982; Gemmrich & Klymak, 2015), in turn elevating
 246 mixing. These regions contribute to the generation of baroclinic IT, in addition

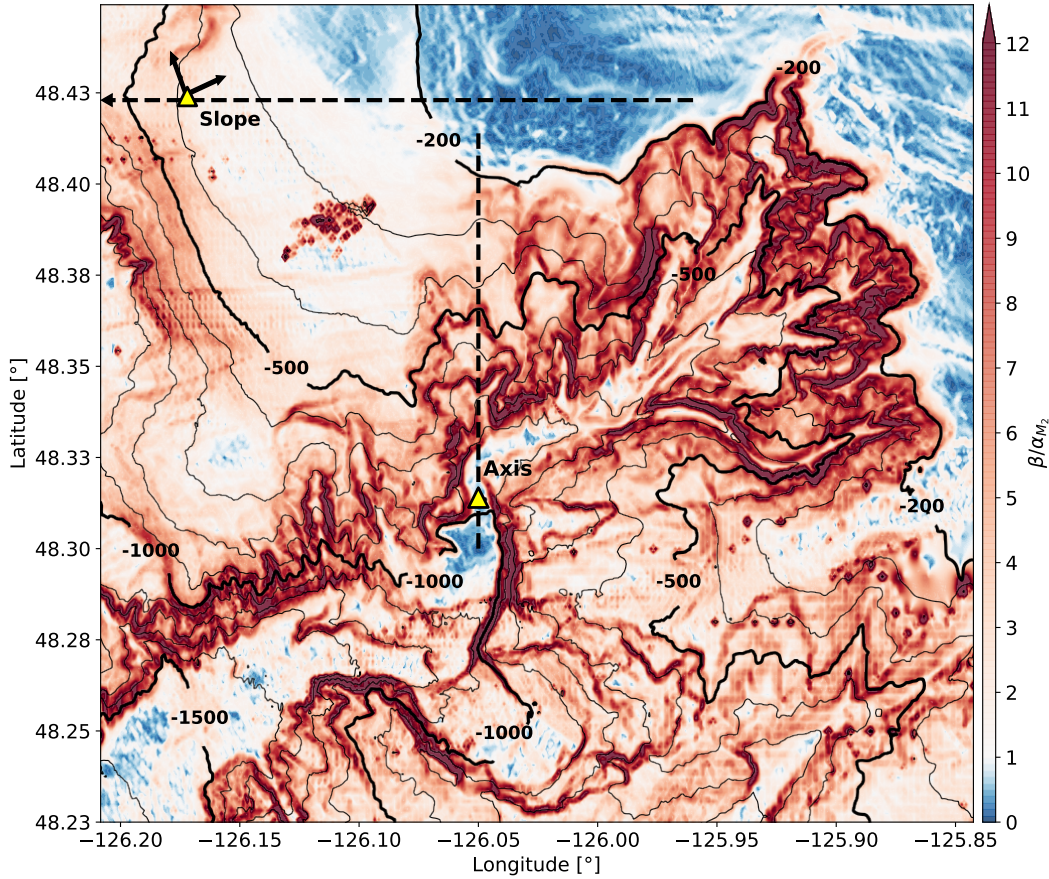


Figure 4. Site map and semidiurnal criticality of Barkley Canyon. Criticality is found by dividing the gradient slope (β) of topography by the depth-dependent semidiurnal propagation angle (α_{M_2}). Most of the region is supercritical (> 1) to the M₂ IT, with notable exceptions on the shelf and canyon floor near the AXIS site. Arrows at the SLOPE site indicate 30° rotation of velocity data to match approximate along-slope (v) direction of mean currents. AXIS data were not rotated, as the along-canyon (v) component is aligned approximately N-S. Dashed black lines indicate topography cross-sections used in Figure 5.

247 to frictional tidal oscillations in non-critical regions (Garrett & Kunze, 2007).
 248 Topographically generated free IT can radiate away baroclinically, potentially
 249 impacting distant topography, dissipating their energy remotely (Kunze et al.,
 250 2012). Dissipation occurs when shoaling IW overturn, isopycnals steepen into
 251 unstable 'internal bores', or barotropic tidal currents generate breaking lee
 252 waves and hydraulic jumps over irregular topography (Martini et al., 2013;
 253 Lamb, 2014). At latitudes where generated IT are trapped to topography,
 254 baroclinic 'shelf waves' may be generated and propagate along the continental
 255 margin, where the bathymetric gradient acts as a restoring force for horizontal
 256 propagation (Crawford & Thomson, 1984; Brink, 1991).

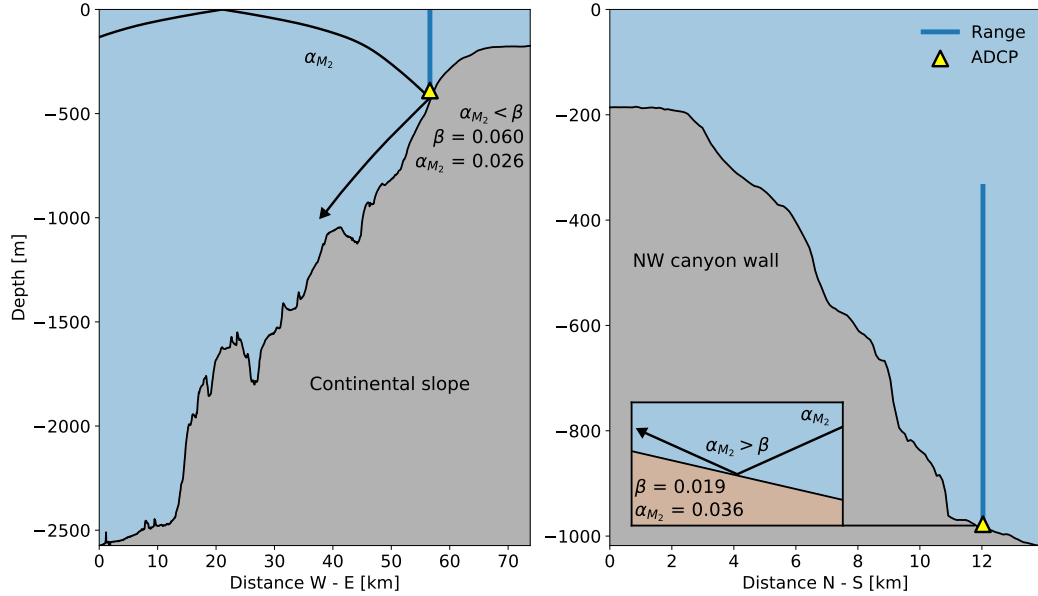


Figure 5. Site topography cross-sections with ray tracing. Depicted are the relative locations for the SLOPE (left) and AXIS (right) moorings. Horizontal cross-sections were taken in the W-E (SLOPE) and N-S (AXIS) directions, represented by the dashed black lines in Figure 4. SLOPE sits below the VICS shelf-break while AXIS is located on the floor of Barkley Canyon (right). An incident ray is shown for M_2 , accounting for depth-dependent stratification, as well as local criticality at each site. α is the angle of propagation, and β the slope of the topography. In general, the SLOPE region is supercritical, while the AXIS region is both subcritical (floor) and supercritical (walls).

257 In addition to topographically generated IW and IT, there is significant in-
 258 put into the oceanic IW field from wind (Alford et al., 2016). NI energy is
 259 deposited into the surface mixed-layer (ML), forcing NI currents that 'strum'
 260 IW modes. In general, the superposition of many modes forms an IW beam
 261 (Lamb, 2014), and the relative rotation and propagation of these modes moves
 262 energy downward to the base of the thermocline, then quickly into the interior
 263 (Zervakis & Levine, 1995). For a flat-bottom basin bounded by the ocean sur-
 264 face, the vertical structure of each IW mode strummed by the NI ML currents
 265 exists as a solution to the Sturm-Liouville equation (Alford & Zhao, 2007):

$$266 \quad \frac{\partial^2}{\partial z^2} \eta(z) + \frac{N^2(z)}{c_n^2} \eta(z) = 0 \quad (4)$$

267 with boundary conditions $\eta(0) = \eta(D) = 0$, where D is the total water depth,
 268 η is surface displacement, n the mode number, and c_n the modal eigenspeed.
 269 Low-modes tend to dominate NI IW energy and largely propagate laterally,
 270 while high-mode energy typically radiates downward (Alford et al., 2016).

271 Propagation of IW and IT can be considered using a simplified 'two-wave

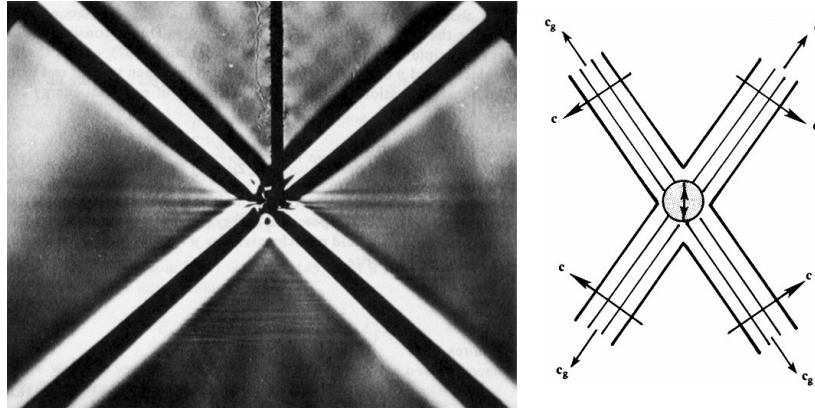


Figure 6. A photograph and graphic showing laboratory evidence for the radiation of 2D IW, from a source. Note the perpendicular phase (here indicated as c) and group velocities, and distinct propagation angles. Adapted from Kundu & Cohen (2008).

model', first discussed in the 19th century by Rusell, Stokes, and Rayleigh, as the superposition of two waves with slightly different wavelengths that form a "slowly varying envelope" (Zhao, 2017) of energy. To describe the waves that comprise this envelope, the horizontal dispersion relation for IW and IT is:

$$\omega^2 = f^2 + c_n^2 k^2 \quad (5)$$

where k is the horizontal wavenumber (Alford et al., 2012; Zhao, 2017). The dispersion relation can be used to find group velocity (c_g) - the velocity of the energetic envelope - and phase velocity (c_p) - the velocity of the individual waves within the envelope (Zhao, 2017), as:

$$c_g = \frac{d\omega}{dk} = \frac{c_n \sqrt{\omega^2 - f^2}}{\omega} \quad (6)$$

and

$$c_p = \frac{\omega}{k} = \frac{\omega c_n}{\sqrt{\omega^2 - f^2}} \quad (7)$$

where phase propagation is both perpendicular and vertically opposite to the motion of the envelope (Figure 6). Similarly, vertical propagation of IW energy, such as for NI IW radiating from the ML into the interior, is described by the vertical group velocity:

$$c_{gz} = \frac{\omega^2 - f^2}{\omega m} \quad (8)$$

where m is the vertical wavenumber (Alford et al., 2012; Alford et al., 2013).

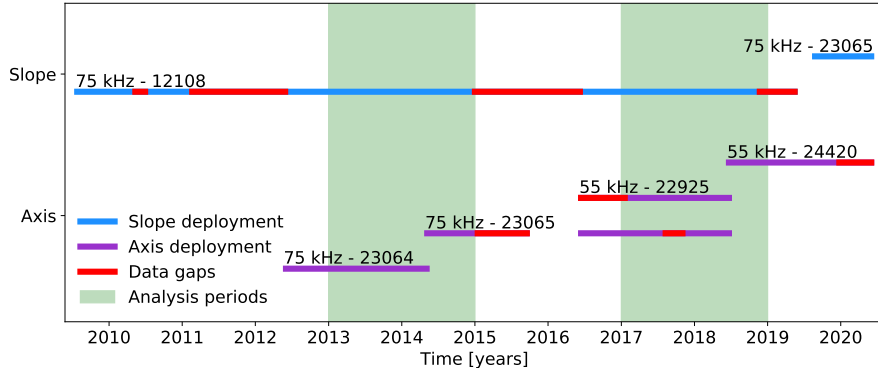


Figure 7. ADCP operating frequency, instrument ID, deployment periods, and data availability for the SLOPE and AXIS moorings. ONC operates and maintains regional instruments as part of the NEPTUNE cabled observatory. Due to maintenance and redeployments, only years with comprehensive overlapping coverage (2013, 2014, 2017, and 2018) were selected for analysis.

290 4 Site and methods

291 Four years of horizontal velocity data were obtained from two Barkley Canyon
 292 moorings. Located approximately 48.33°N 126.03°W, the Barkley Canyon re-
 293 gion is 75 km southwest of the coast of Vancouver Island, incising the con-
 294 tinental slope and VICS (Figure 4). Barkley Canyon is a winding canyon
 295 up to 6 km wide and 13 km long, with an adjacent shelf-break region at
 296 around -150 m depth. Moored acoustic Doppler current profilers (ADCP)
 297 emit acoustic beams that triangulate Doppler shifts in the water column to
 298 provide horizontal (u , v) and vertical (w) velocity time series data for Ocean
 299 Networks Canada's (ONC) NEPTUNE cabled observatory. The placement of
 300 the Barkley Canyon ADCP moorings across both continental slope and canyon
 301 topography allows for spatial comparison of coinciding IW events, while ONC's
 302 Oceans 2.0 data portal offers over a decade of processed data, allowing for typ-
 303 ically difficult analysis of long-term variability.

304 Two ADCP moorings were selected for this study, located at upper continental
 305 slope (SLOPE) and canyon-floor (AXIS) sites (Figure 4). The SLOPE platform
 306 sits below the VICS shelf-break at a depth of -378 m (Figure 5), 15 km north-
 307 west of Barkley Canyon, employing primarily Teledyne RDI 75 kHz Workhorse
 308 Long Ranger ADCPs. The AXIS platform is located at a narrow north-south
 309 channel on the floor of Barkley Canyon, about midway along its length at
 310 a sharp bend, and a depth of -968 m (Figure 5), employing similar 75 kHz
 311 instruments, as well as 55 kHz Nortek Signature55 ADCPs. The Teledyne RDI
 312 75 kHz Workhorse Long Ranger instruments were set to a vertical resolution

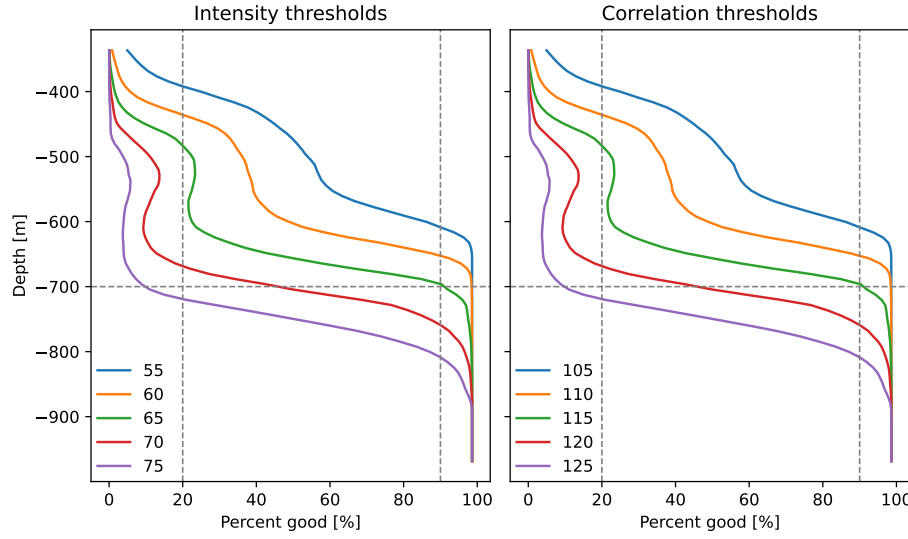


Figure 8. Backscatter intensity and beam correlation percent-good vertical profiles for various QC thresholds. The green line in each was selected as the ideal threshold value due to the step-function-like steepness of the profile at 20% and 90%, in addition to the qualitative removal of depth-dependent processing artefacts and near-surface side-lobe contamination when used together as a mask.

of 8 m depth bins, and a continuous sampling rate of 2 seconds. The 55 kHz Nortek Signature55 instrument was set to a vertical resolution of 20 m depth bins, and a pulsed sampling rate of six 18-second interval pings followed by a 4.5-minute delay. For these sites, overlapping data coverage of good quality (e.g. minimal data gaps) is during 2013, 2014, 2017, and 2018 (Figure 7), due to ONC redeployment and maintenance schedules.

An initial quality check of backscatter intensity and beam correlation was performed for the raw data (Figure 8), yielding quality thresholds of 65 and 115 counts, respectively. There is some seasonal variation in the vertical percent-good profiles based on these thresholds, notably in the fall, likely associated with seasonality of biological scatterers higher in the water column. Time-averaged profiles indicate regions of good data ($\geq 90\%$ good) below -50 m at SLOPE, and below -700 m at AXIS. Masking above these depths avoids near-surface side-lobe contamination, and depth-dependent processing artefacts - non-physical high-frequency spikes in power spectra obvious above about -600 m. The expected range for AXIS instruments is well above -700 m, so up to -600 m is retained in plots for reference, and a dashed line at -700 m indicates the upper extent of the analysis region. For most of the analysis the 2-second high-frequency data were averaged to 15-minute blocks. All supplemental processing materials, including Python code and plots, are available in a project

³³³ GitHub repository (Anstey, 2022).

³³⁴ At SLOPE, to better match the physical cross-slope angle of approximately 30°,
³³⁵ horizontal velocity data were rotated using a standard rotation matrix:

$$\text{336} \quad u_{rot} = u\cos(\theta) - v\sin(\theta) \quad (9)$$

$$\text{337} \quad v_{rot} = u\sin(\theta) + v\cos(\theta) \quad (10)$$

³³⁹ where θ is the rotation angle in radians. u is referred to as cross-slope, and v
³⁴⁰ as along-slope (Figure 4). At AXIS, the along-canyon (v) direction is already
³⁴¹ approximately north-south, and u is referred to as cross-canyon.

³⁴² To account for depth-dependent stratification in spectral analysis, horizontal
³⁴³ velocity data were WKB-scaled as:

$$\text{344} \quad u_{WKB}(z) = u(z)\sqrt{\frac{N_0}{N(z)}} \quad (11)$$

³⁴⁵ and for energy density as:

$$\text{346} \quad \phi_{WKB}(z) = \phi(z)\frac{N_0}{N(z)} \quad (12)$$

³⁴⁷ with a reference buoyancy frequency of $N_0 = 2.53 \times 10^{-3}$ rad s⁻¹ averaged
³⁴⁸ around -900 m (Althaus et al., 2003). Buoyancy data were determined from
³⁴⁹ climatology data obtained from the nearby (20 km south of Barkley Canyon)
³⁵⁰ station LB14. Data were sampled annually in May and September, during
³⁵¹ Fisheries and Oceans Canada (DFO) La Perouse cruises, casting down to -1180
³⁵² m. Depth profiles were obtained for temperature, pressure, and salinity, $S(z)$,
³⁵³ to find potential density, $\rho_\theta(z)$, following the UNESCO EOS 80 polynomial
³⁵⁴ (Mamayev et al., 1991). Depth-dependent buoyancy was then determined
³⁵⁵ as in Equation 1 (Figure 9). There is little inter-annual variability in the
³⁵⁶ buoyancy depth profiles.

³⁵⁷ Component-wise power spectral density (PSD) was determined from the WKB-
³⁵⁸ scaled horizontal velocity data for each depth bin, using a Welch spectrogram
³⁵⁹ process with a Hanning window of 256 data-points (~ 2.7 days), 50% overlap,
³⁶⁰ and detrended in time to avoid a 0 Hz offset. Short 1.3 day and long 5.3 day
³⁶¹ spectra were also computed. The noise floor of each instrument was deter-
³⁶² mined from the standard error of the mean relative to instrument sampling
³⁶³ intervals and uncertainties from Nortek and Teledyne RDI. 95% confidence
³⁶⁴ intervals were determined using a chi-squared method.

³⁶⁵ For rotational dependence, rotary power spectra were determined as for PSD,
³⁶⁶ using a modified spectrogram process based on the work of Gonella (1972)

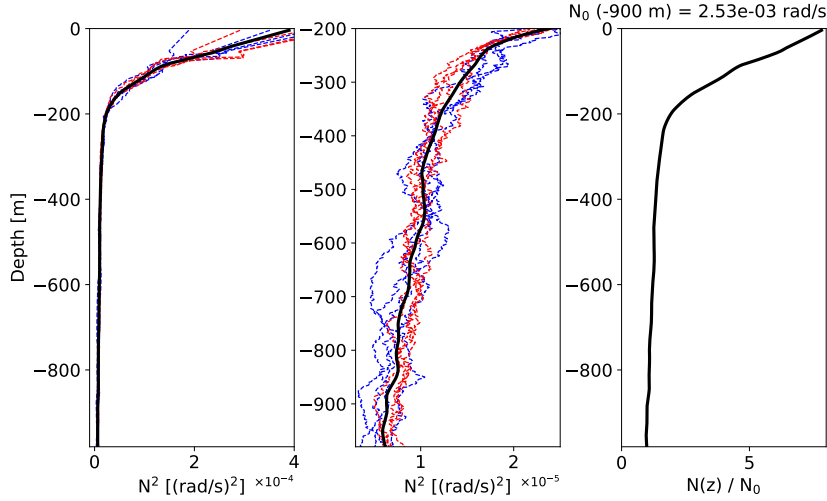


Figure 9. N^2 parameter and WKB scaling factor. Buoyancy results were smoothed and averaged for the four analysis years of station LB14 CTD data, and are displayed through the water column (left) and below -200 m (centre). Casts were taken in May (blue) and September (red). A WKB scaling factor (right) was determined for use in Equation 12, based on N_0 averaged around -900 m.

and Thomson and Emery (2014). To summarise, the adjustment to find the counter-clockwise (CCW) and clockwise (CW) components of a complex horizontal velocity vector, $\mathbf{w}(t) = u(t) + iv(t)$, is the addition or subtraction of twice its quadrature spectrum, Q_{uv} , as:

$$\text{CCW} = \frac{1}{2}[S_{uu} + S_{vv} + 2Q_{uv}] \quad (13)$$

$$\text{CW} = \frac{1}{2}[S_{uu} + S_{vv} - 2Q_{uv}] \quad (14)$$

where S_{uu} and S_{vv} are the typical complex autospectra used for PSD (Thomson & Emery, 2014). In general, a stronger CW component indicates downward propagation of energy, and vice-versa.

The open-ocean GM IW spectrum was determined for local parameters of $f = 1.09 \times 10^{-4} \text{ rad s}^{-1}$, $g = 9.81 \text{ m s}^{-2}$, and N_0 , along with canonical values for the surface-extrapolated buoyancy frequency ($N_{GM} = 5.24 \times 10^{-3} \text{ rad s}^{-1}$), e-folding scale of $N(z)$ ($1.3 \times 10^3 \text{ m}$), mode scale number $j^* = 3$, and dimensionless IW energy parameter $E = 6.3 \times 10^{-5}$, as in Munk and Wunsch (1998). The directional GM spectrum was adapted to rotary form through application of the rotary consistency relation, as described in Section 3 (Levine, 2002; Polzin & Lvov, 2011).

For wind forcing of NI IW, a slab model was conducted as in D'Asaro (1995)

and Alford (2001), providing a simplified version of the ML response to NI wind forcing (Alford et al., 2016). Though simple, the model is continuously being improved to better account for non-homogeneous internal ML processes, and ML to pycnocline energy transfer (Alford & Zhao, 2007; Jarosz et al., 2007; Alford et al., 2016; Zheng et al., 2017; Voelker et al., 2020; Alford, 2020). From surface wind time series, wind stress is calculated as in Garratt (1977):

$$\tau_0 = \rho C_D V(z)^2 \quad (15)$$

where ρ is the density of air (approximated as 1), $V(z)$ is the complex wind velocity vector, and C_D is the characteristic drag coefficient determined by:

$$C_D \times 10^3 = 0.51V^{0.46} \quad (16)$$

For appropriate slab model seasonality a ML of seasonally varying depth, H , must be considered. Assuming a null initialisation parameter u_{I1} at time t_1 , wind generated slab layer currents at time t_2 are then computed as:

$$u_{I2} = u_{I1} e^{-\omega \Delta t} - \frac{T_t}{H \omega^2} (1 - e^{-\omega \Delta t}) \quad (17)$$

where a damped rotation frequency, ω , is determined as:

$$\omega = r + i f \quad (18)$$

with $r = 0.15f$ is an artificial damping parameter, as defined in Alford (2001), and:

$$T_t = \frac{\Delta T}{\Delta t} \quad (19)$$

is related to the complex stress vector:

$$T = \frac{\tau_x + i \tau_y}{\rho_{ML}} \quad (20)$$

where $\rho_{ML} = 1024 \text{ kg m}^{-3}$ is the average density of the ML. The slab currents are then band-passed for their NI component, u_{NI} .

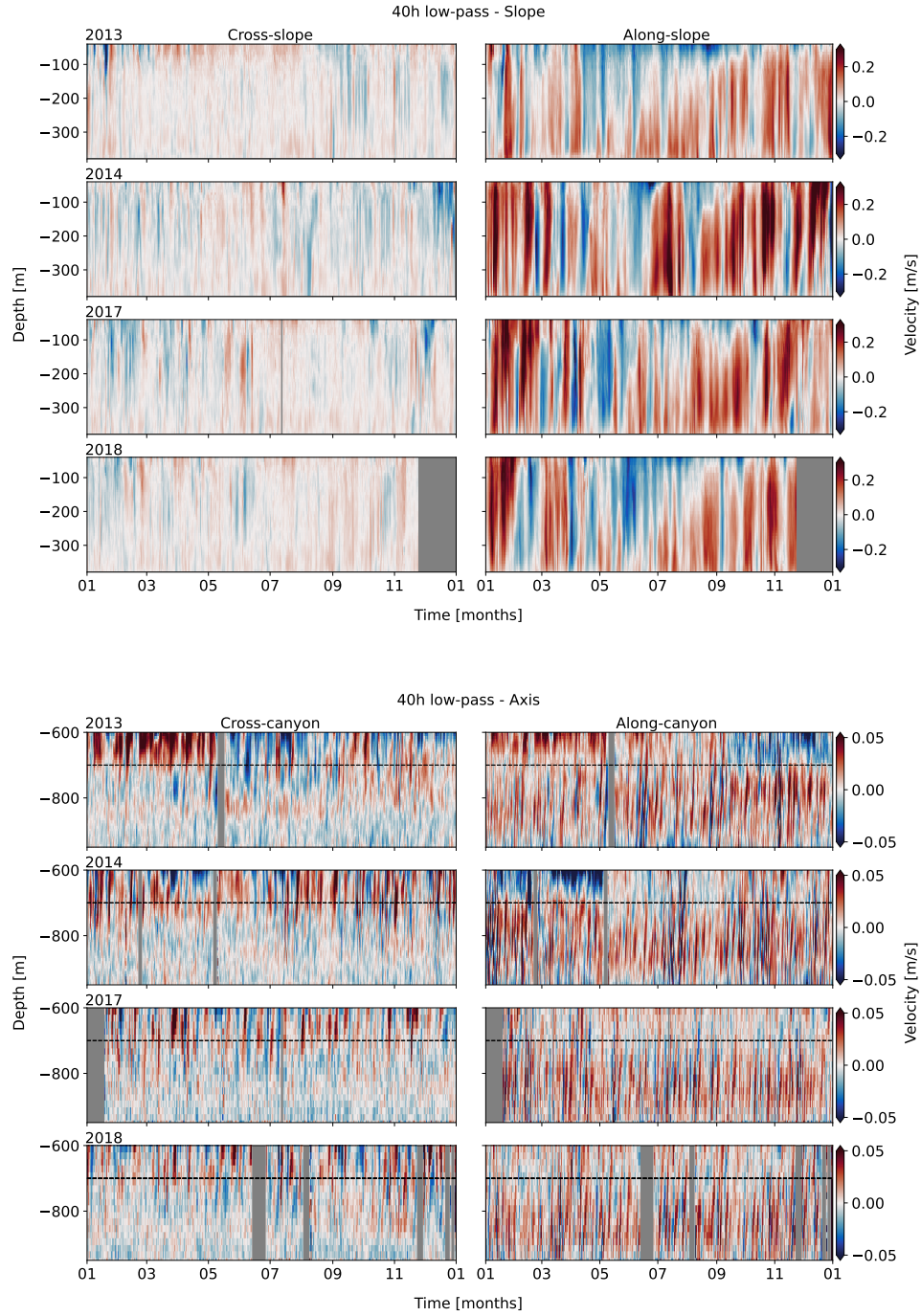


Figure 10. 40-hour low-pass horizontal velocity data for SLOPE (top) and AXIS (bottom). Components are separated as cross- (left) and along-slope/canyon (right). At AXIS, the dashed line is the upper limit of the analysis depths (-700 m). There is a clear seasonal cycle in the along-slope component at SLOPE, while seasonality is less apparent in the dominantly along-canyon flow at AXIS.

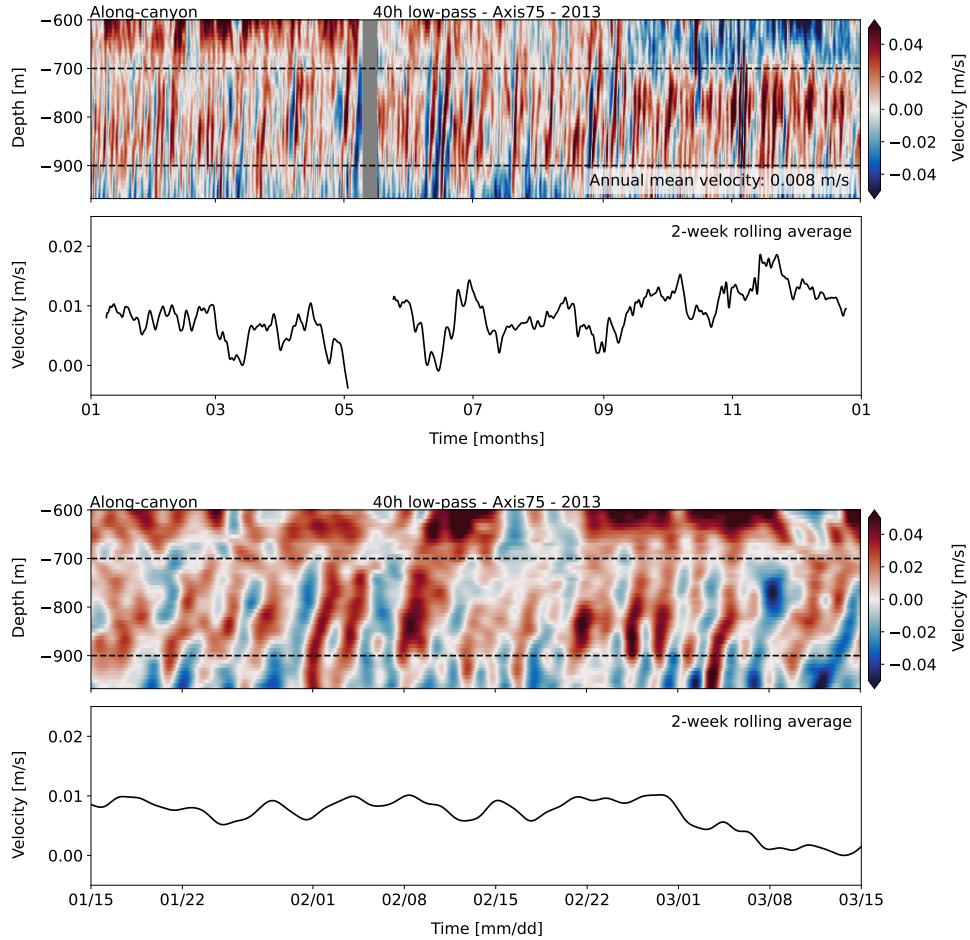


Figure 11. 40-hour low-pass horizontal velocity data showing along-canyon mean currents for AXIS, in 2013 (top) and in a two-month snapshot (bottom). Mean up-canyon flow is within the dashed lines. A thin near-bottom layer of mean down-canyon flow is below.

409 5 Results

410 5.1 Observations

411 5.1.1 Mean currents

412 Regional low-frequency mean currents are inter-annually consistent, topo-
 413 graphically guided, and seasonally site-dependent (Figure 10). To identify
 414 long-term mean currents, a 40-hour, 8th-order, digital low-pass Butterworth
 415 filter was applied to the horizontal velocity data. There is little inter-annual
 416 variability in mean currents, though each site has unique seasonality. At
 417 SLOPE, mean currents below -50 m are as expected for this portion of the Cali-
 418 fornia current system (Figure 10): generally poleward along-slope (up to > 0.2

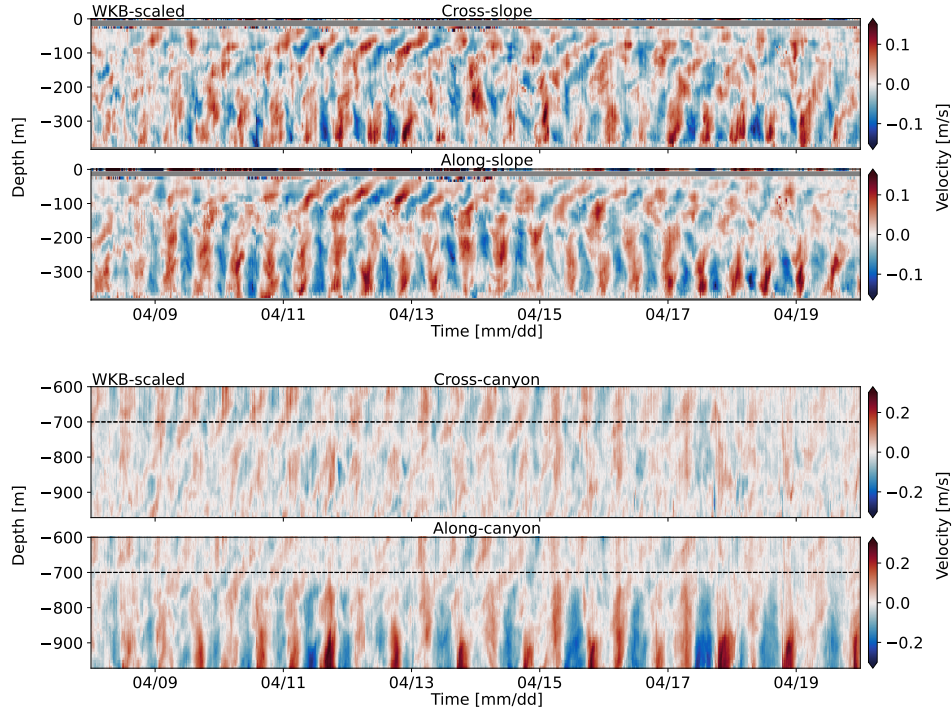


Figure 12. 40-hour high-passed WKB-scaled horizontal velocity data for SLOPE (top) and AXIS (bottom), in April 2013. Components are separated as cross- (upper) and along-slope/canyon (lower). There are IW and IT of varied frequency, non-uniform vertical structure, and depth-dependence.

419 m s^{-1}) through depth, with a quick transition to upwelling-favourable equa-
 420 torward flow in the late-spring (April/May), with the deep poleward currents
 421 shoaling by fall (Thomson & Krassovski, 2015). In the canyon, mean currents
 422 between -700 and -900 m are consistently positive (up-canyon/landward) up
 423 to $> 0.05 \text{ m s}^{-1}$, with two-week rolling depth-average velocities up to 0.02 m s^{-1} ,
 424 and annual means of $0.007 - 0.010 \text{ m s}^{-1}$. Two-month snapshots show the
 425 up-canyon flow is comprised of pulses of velocity propagating upward from the
 426 bottom with periodicity of about a week (Figure 10 - lower). This periodic-
 427 ity is consistent both seasonally and inter-annually (not shown). In contrast,
 428 there is mostly down-canyon flow $< 50 \text{ m}$ above bottom.

429 5.1.2 High-passed currents

430 High-passed (< 40 -hour) velocity data show variable periodicity and vertical
 431 structure. Subtracting the 40-hour low-pass currents from the total yields
 432 residual high-passed currents - flows with periodicity less than 40 hours (Fig-
 433 ure 12). A two-week snapshot during the annually recurring April/May mean
 434 current transition reveals the presence of tidal and NI IW with non-uniform

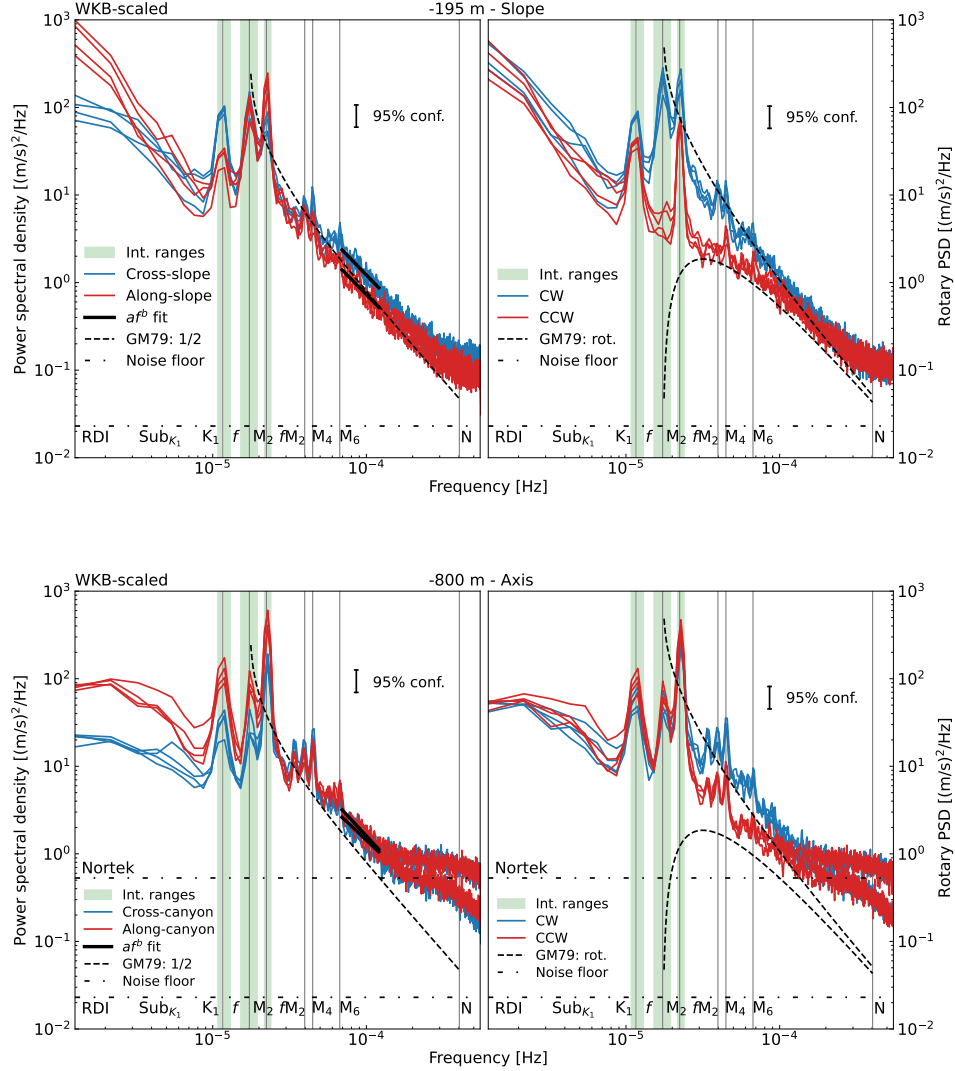


Figure 13. Mid-depth annual PSD (left) and rotary (right) spectra of WKB-scaled horizontal velocity data, for SLOPE (top) and AXIS (bottom). Each line of the same colour is a different year. For PSD, cross- (blue) and along-slope/canyon (red) components are shown. For rotary, CW (blue) and CCW (red) components are shown. 95% confidence intervals are indicated by the upper-right black bar. Dotted lines show instrument noise floors. Frequency constituents with integration ranges for primary tidal and NI bands (vertical lines and green shading) are shown. For PSD, thick black lines indicate fits to high-frequency continuum range, and the dashed line is the GM79 spectrum (1/2 amplitude). For rotary, the GM79 spectrum is in rotary components (CW upper). Spectra at both sites are characteristically red, with prominent tidal and NI peaks.

435 vertical structure. At the SLOPE site, high-passed currents exceed 0.1 m s^{-1}
 436 in both cross- and along-slope directions, and there is periodic upward propa-

437 gation above -250 m depth (about 150 m above bottom). At AXIS, high-pass
438 currents are strongest below -750 m (about 250 m above bottom), exceeding
439 0.2 m s^{-1} and mostly along-canyon, with increased non-uniformity in the
440 vertical structure above.

441 Annual mid-depth (-195 m and -800 m) velocity power spectra at each site show
442 strong tidal and NI influence (Figure 13), with site- and frequency-dependent
443 topographic guidance. Inter-annual variability is minimal (each line of the
444 same colour is a different year), with annual spectra overlapping within a 95%
445 confidence interval. The low-frequency sub-diurnal broadband ranges up to
446 $1.00 \times 10^{-5} \text{ Hz}$. The most defined spectral peaks are of the diurnal ($1.16 \times$
447 10^{-5} Hz), NI ($1.73 \times 10^{-5} \text{ Hz}$), and semidiurnal ($2.24 \times 10^{-5} \text{ Hz}$) frequencies.
448 Closely associated tidal constituents (such as S_2 and M_2) were identified in
449 high frequency-resolution spectra (not shown) as having similar topographic
450 and seasonal responses, so shorter spectral windows are used for better seasonal
451 resolution. Tidal constituents are therefore referred to generally (e.g. diurnal).
452 The high-frequency IW continuum band ($7.00 \times 10^{-5} - 1.20 \times 10^{-4} \text{ Hz}$) ranges
453 between M_6 ($\sim 6.8 \times 10^{-5} \text{ Hz}$) and an apparent energy build-up occurring near
454 N (between $2.00 \times 10^{-4} - 1.00 \times 10^{-3} \text{ Hz}$), discussed further in Section 5.2.6.

455 At SLOPE (Figure 13 - upper), the low-frequency (sub-diurnal) flow is almost
456 entirely along-slope (an energy ratio of up to 10:1, compared to cross-slope),
457 with strength increasing inversely to frequency (Figure 13), indicating the
458 importance of variability in the along-shelf currents. The diurnal constituent
459 is strongest cross-slope (over 3:1), similar to observations by Crawford (1984;
460 Crawford & Thomson, 1984) who noted diurnal tidal ellipses were rotated
461 cross-slope over the Vancouver Island continental slope. The NI peak is equally
462 distributed (1:1), indicative of rotary motion, and is indeed dominant in its
463 CW (downward) rotary component, as expected in the northern hemisphere.
464 The semidiurnal constituent is somewhat stronger along-slope (up to 2:1),
465 again suggesting the influence of along-shelf currents. The high-frequency
466 continuum is slightly stronger cross-slope, and trails off slightly whiter than
467 the expected open-ocean GM slope of -2 (discussed in Section 5.2.5). The
468 apparent near- N build-up is partially resolved as a whitening effect, and is
469 better observed in the raw (2-second) spectra.

470 At AXIS (Figure 13 - lower), compared to SLOPE, sub-diurnal power is weaker
471 at frequencies below $4.00 \times 10^{-6} \text{ Hz}$ (Figure 13). Sub-tidal, tidal, and NI bands
472 all trend towards along-canyon (from 3:1 at sub-diurnal, to 2:1 at semidiurnal,
473 compared to cross-canyon), rectilinear motions. This is surprising for the NI
474 band as a strong CW component is expected in most observations, suggesting
475 strong topographic guidance of tidal and NI currents. Above the semidiurnal

476 peak, the super-tidal and high-frequency continuum ranges are mostly CW
 477 (about 2:1), suggesting the high-frequency flows are less guided of the relatively
 478 broad canyon. Compared to SLOPE, the near- N energy build-up is obvious in
 479 2013 and 2014, while in 2017 and 2018 the Nortek 55 kHz noise floor masks
 480 the effect.

481 5.1.3 Depth dependence

482 At each site, there is adjustment of spectral power near topography that is
 483 frequency-dependent. The WKB-scaled PSD and rotary spectra were time-
 484 averaged for annual 2D depth-frequency analysis (Figure 14). Results show
 485 a general increase (or decrease, for NI at SLOPE) in spectral energy (over an
 486 order of magnitude) in a concentrated layer < a few hundred metres above
 487 bottom.

488 At SLOPE (Figure 14 - upper), the sub-diurnal, tidal, and high-frequency con-
 489 tinuum bands show near-bottom intensification of IW energy. In contrast, the
 490 NI band is attenuated approaching the sea floor, below an average depth of
 491 -250 m (130 m above bottom). Near-slope adjustment is up to a factor of 10,
 492 compared to background energy. Most bands show intensification most obvi-
 493 ously in the along-slope component, suggesting strong topographic influence,
 494 while the NI band is most obviously attenuated in its CW rotary component.

495 At AXIS (Figure 14 - lower), most constituents show rectilinear, along-canyon
 496 near-bottom intensification, below an average depth of -750 m depth (230 m
 497 above bottom). Near-bottom adjustment is up to a factor of 100, compared
 498 to background energy. The sub-diurnal and diurnal intensification is entirely
 499 along-canyon, with little to no power in the cross-canyon direction. The NI
 500 band, in contrast to the CW energy attenuated near the sea floor at SLOPE, has
 501 bottom-intensified flow that is almost entirely along-canyon (discussed further
 502 in Section 5.2.3). The semidiurnal intensification is strongly along-canyon,
 503 but with a medium-strength cross-canyon signal that is sharply attenuated
 504 below -900 m. High-frequency continuum strength varies between cross- and
 505 along-canyon.

506 A vertical scale analysis roughly agrees with the qualitative observations of
 507 enhanced layer thickness. Gemmrich and Klymak (2015) found that mode-1
 508 IW incident on sloped topography can induce a near-bottom turbulent flow
 509 layer, and that the vertical scale of the effect can be approximated as:

$$510 \quad H \approx \frac{\pi U}{N} \quad (21)$$

511 where U is the forcing by horizontal velocity. For strong near-bottom velocities
 512 (Figure 12) and approximate buoyancy values (Figure 9) for near-topography

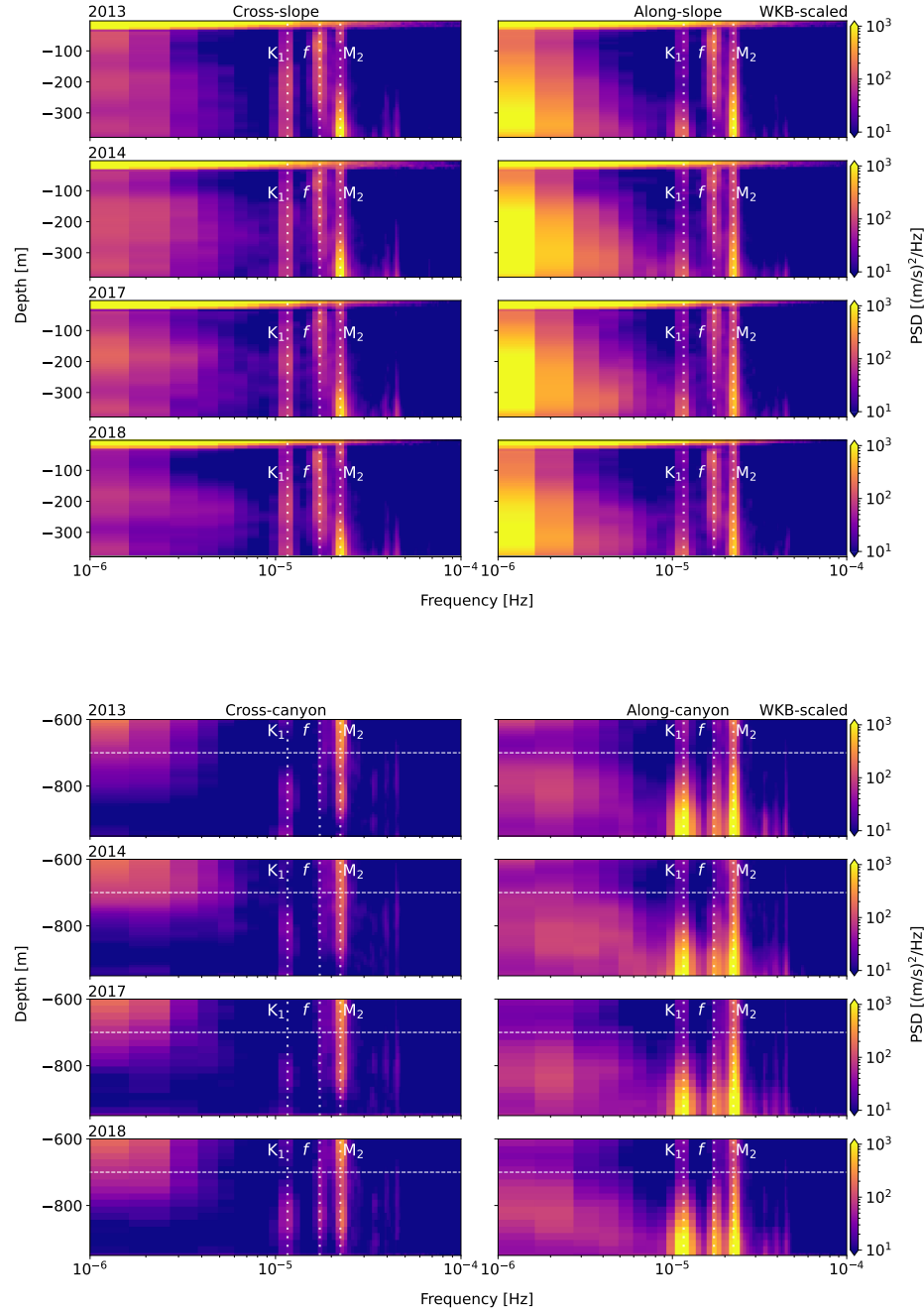


Figure 14. Depth-frequency PSD for SLOPE (top) and AXIS (bottom), determined from WKB-scaled horizontal velocity data. Components are separated as cross- (left) and along-slope/canyon (right). There is near-bottom intensification of individual frequency constituents (and near-bottom attenuation of the NI band, at SLOPE).

513 depths at SLOPE ($U \approx 0.15 \text{ m s}^{-1}$ and $N \approx 3.5 \times 10^{-3} \text{ rad s}^{-1}$, at -350 m)
514 and AXIS ($U \approx 0.25 \text{ m s}^{-1}$ and $N \approx 2.5 \times 10^{-3} \text{ rad s}^{-1}$, at -900 m), estimates
515 yield vertical scales of 135 m and 314 m, respectively. Results are similar to
516 the qualitative thickness of 130 m above bottom at SLOPE, somewhat greater
517 than the observed 230 m above bottom at AXIS, and agree with the results of
518 Gemmrich and Klymak (2015) for similar forcing and stratification. It should
519 be noted that the CTD climatology data are from a nearby open-ocean site,
520 and so do not reflect changes in stratification near topography.

521 **5.2 Band-integrated depth and seasonal changes**

522 There is frequency-dependent variability in the seasonality of the near-topography
523 enhanced energy (and attenuation for NI at SLOPE). Little inter-annual vari-
524 ability is observed, noted only in the more intermittent sub-diurnal and NI
525 seasonality. WKB-scaled PSD and rotary spectra were integrated over band-
526 widths comprising each constituent's peak or frequency range (shown as shaded
527 green in Figure 13), for each depth bin, yielding 2D estimates of 'depth-band'
528 power. Constituent integration ranges are sub-diurnal ($\leq 1.08 \times 10^{-5} \text{ Hz}$),
529 diurnal ($1.08 - 1.30 \times 10^{-5} \text{ Hz}$), NI ($1.52 - 1.95 \times 10^{-5} \text{ Hz}$), semidiurnal
530 ($2.17 - 2.39 \times 10^{-5} \text{ Hz}$), high-frequency continuum ($7.00 \times 10^{-5} - 1.20 \times 10^{-4}$
531 Hz), and near- N ($2.00 \times 10^{-4} - 1.00 \times 10^{-3} \text{ Hz}$).

532 **5.2.1 Sub-diurnal**

533 At SLOPE (Figure 15 - upper), seasonality of sub-diurnal ($\leq 1.08 \times 10^{-5} \text{ Hz}$)
534 energy consists of intermittent pulses, strongest in fall and winter, and is one
535 of few observations that is not inter-annually consistent. At AXIS (Figure
536 15 - lower), seasonality is weak, showing an occasional fall or winter pulse. A
537 seasonal forcing analysis of the sub-diurnal constituent is inconclusive, as there
538 is no correlation with wind or tides (not shown), or the expected low-frequency
539 along-slope mean currents (Figure 10). Low-frequency flows can be affected
540 by a variety of physical processes near slope, shelf, and canyon topography,
541 such as upwelling and shelf waves (Cummins, 2000; Thomson & Emery, 2014;
542 Thomson & Krassovski, 2015), and is likely a complex combination of regional
543 physical processes. Further forcing analysis for the sub-diurnal range is beyond
544 the scope of this study.

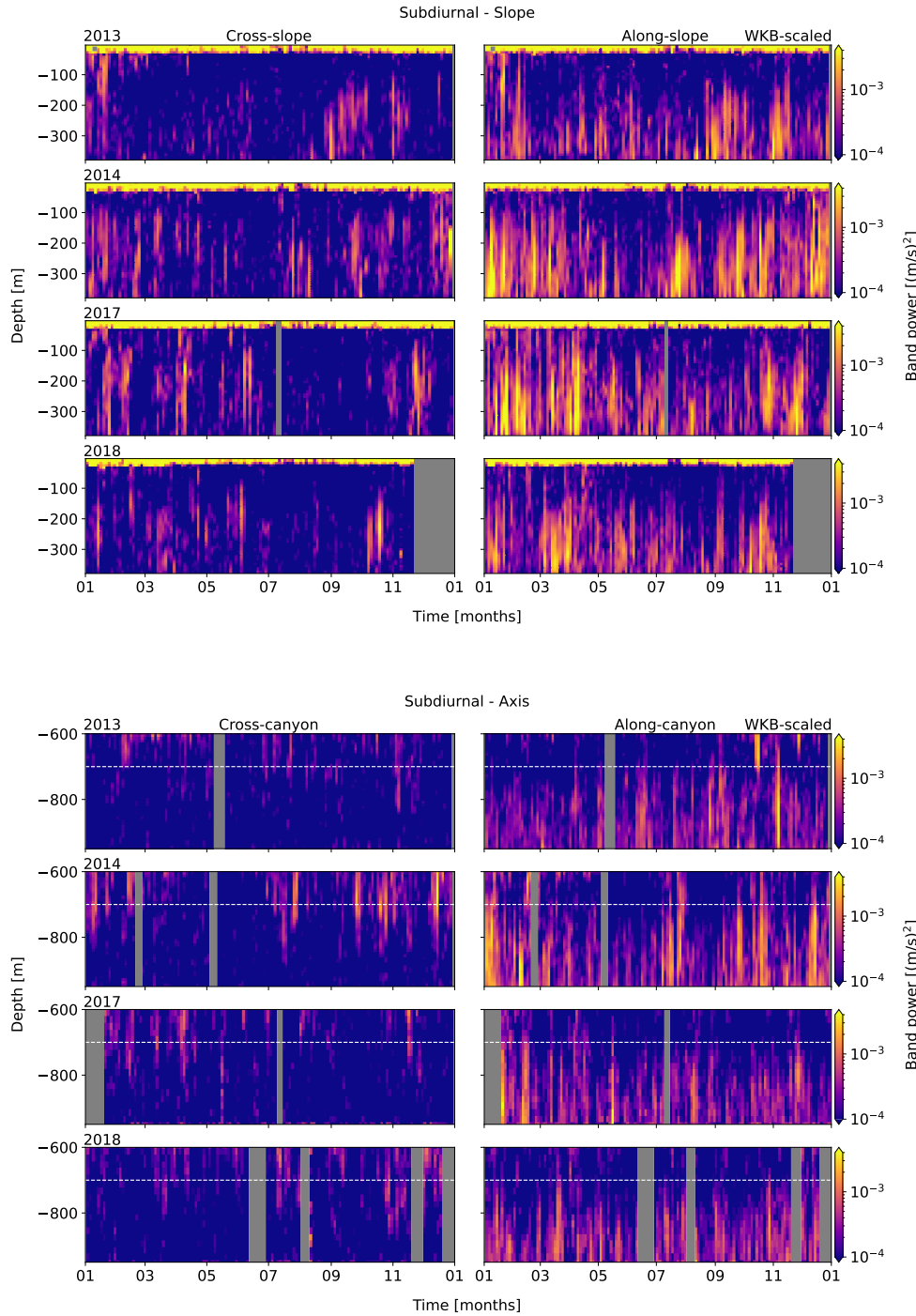


Figure 15. Band-integrated sub-diurnal PSD for SLOPE (upper) and AXIS (lower), from WKB-scaled horizontal velocity data. Cross- (left) and along-slope/canyon (right) components are shown. Each row represents an analysis year, labelled at upper-left.

545 **5.2.2 Diurnal**

546 Diurnal ($1.08\text{--}1.30 \times 10^{-5}$ Hz) seasonality at SLOPE (Figure 16 - upper) is inter-
547 annually consistent, with elevated energy late-spring through summer (months
548 5-8) and again (weaker) in the fall/early-winter (months 11-1). Seasonality at
549 AXIS is not readily apparent (Figure 16 - lower).

550 The diurnal band is in sync with the local barotropic spring-neap cycle, fort-
551 nightly and seasonally, at both sites (Figure 17). Surface-level data were
552 obtained from the Canadian Hydrographic Service (CHS) gauge in Tofino,
553 approximately 90 km due north of Barkley Canyon, as hourly time-series of
554 deviation from chart datum, and power spectra diurnally band-passed using
555 a similar process as for velocity observations. Comparing long-term season-
556 ality, the Tofino barotropic spring-neap amplitudes peak in months 6-8 and
557 11-2, corresponding well with the diurnal observations at Barkley Canyon, and
558 are consistent inter-annually. Fortnightly, 3-month phase-lag correlations were
559 performed between the depth-mean diurnal power and surface-level time series,
560 for months 1-3, 4-6, 7-9, and 10-12, each year. Phase-lag correlations range
561 from 0 to 1 day at SLOPE (inter-annual average of 0.5 days), and 0 to 2 days
562 at AXIS (inter-annual average of 1.1 days) - both less than the time-resolution
563 of the spectral estimates (~ 2.7 days) used for correlations. It should be noted
564 that AXIS estimates are only partial-depth and cannot fully resolve barotropic
565 water-column motions, potentially contributing to observed phase offsets. Re-
566 gardless, the diurnal observations are mostly in sync with both the fortnightly
567 and seasonal local barotropic spring-neap cycle, indicating they are largely
568 generated locally, within about 200 km Barkley Canyon (discussed in Section
569 6.2).

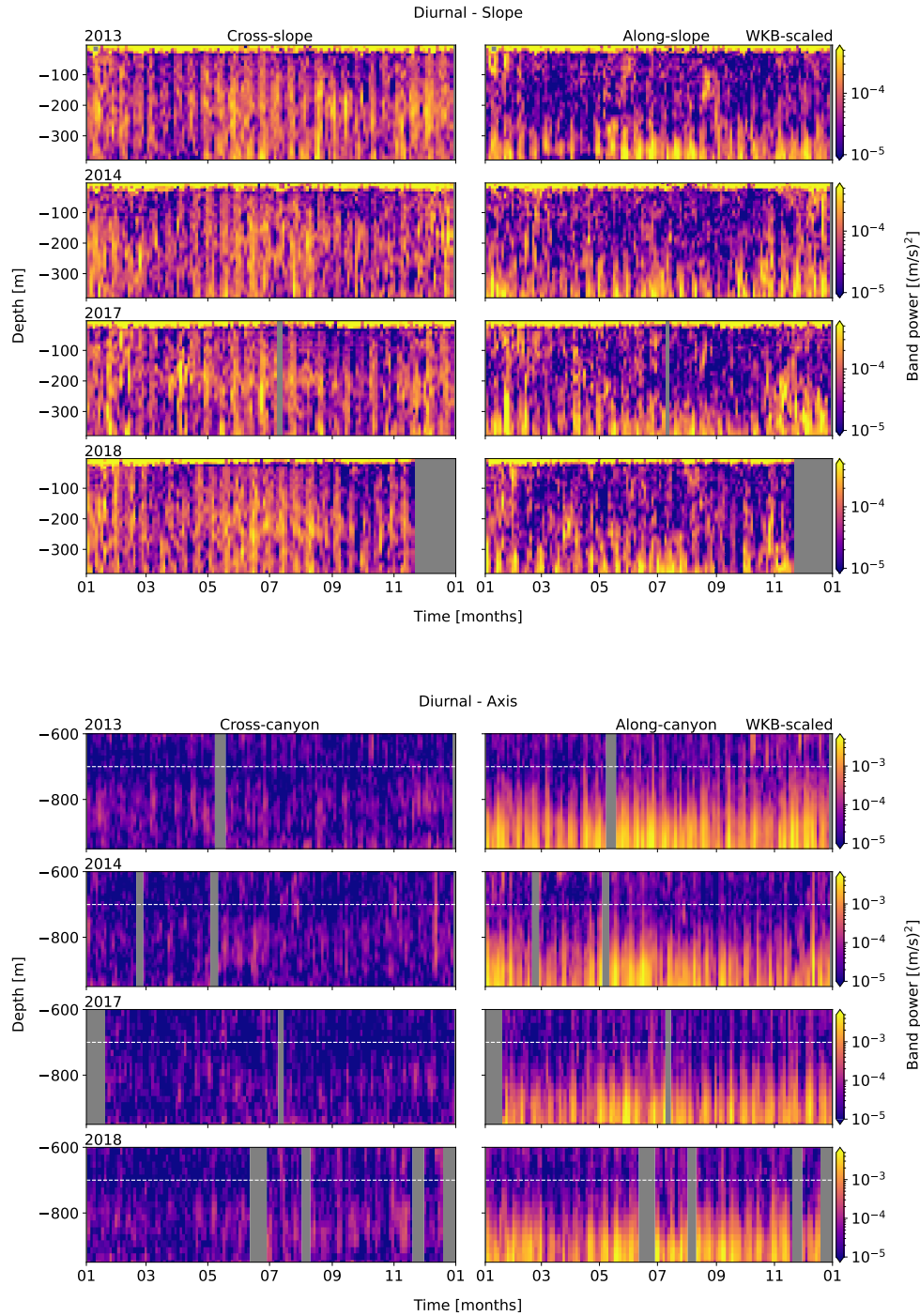


Figure 16. Band-integrated diurnal PSD for SLOPE (upper) and AXIS (lower), from WKB-scaled horizontal velocity data. Cross- (left) and along-slope/canyon (right) components are shown. Each row represents an analysis year, labelled at upper-left.

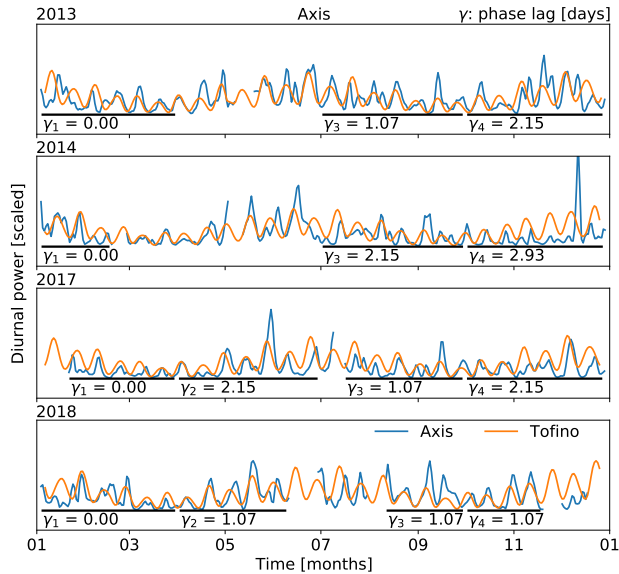
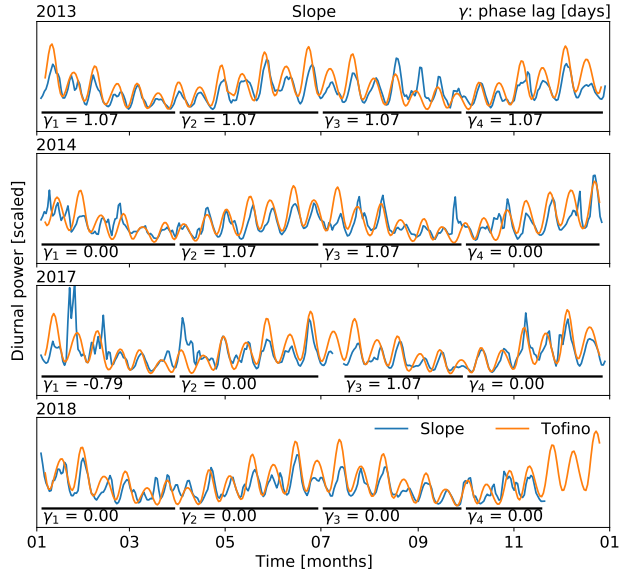


Figure 17. Diurnal barotropic forcing comparison. Phase-lag correlation and amplitude (scaled) comparisons for band-integrated power of diurnal surface level data (Tofino, orange) and WKB-scaled depth-mean diurnal power (blue) at SLOPE (top) and AXIS (bottom). Black bars indicate seasonal correlation ranges. There is a consistent yet minor phase-lag, less than the time-scale of each spectral estimate.

570 **5.2.3 Near-inertial**

571 At SLOPE (Figure 18 - upper), near-surface NI ($1.52 - 1.95 \times 10^{-5}$ Hz) sea-
572 sonality is highly intermittent, with pulses occurring most likely in the fall
573 and early-winter, though possible year-round. Some of the fall and winter NI
574 events seen in the SLOPE data are also clear deep in AXIS observations (Figure
575 18 - lower). Seasonality is inter-annually consistent, but specific events are
576 not.

577 For prominent pulses at SLOPE, there are periods of downward propagation
578 of NI energy from the ML (above -50 m) to about -100 m, lasting up two
579 weeks, after which the deep response increases quickly. At AXIS, the timing
580 of observed pulses near the bottom appears to correspond to the delayed deep
581 response at SLOPE. Figure 19 shows a sample event in September of 2014. A
582 surface event deposits energy into the ML on September 3. Over the next 8
583 days, energy is transferred down to about -100 m. Upon reaching this depth,
584 there is an immediate deep response. Energy continues to pool around -100 m,
585 maintaining the deep response until September 14, when NI energy appears
586 to have dissipated. There are many of these events each year, enumerated in
587 Figure 20. The fall sees the most events, all of which are short lived, from 7-9
588 days, while the winter has the longest events, up to 16-18 days.

589 Slab model results indicate NI forcing is qualitatively linked with regional wind
590 events, mostly in the fall and early-winter (Figure 21). Wind data were ob-
591 tained from the closest Fisheries and Oceans Canada (DFO) weather buoy, La
592 Perouse (46206, 50 km north of Barkley Canyon), as time series of magnitude
593 and direction. Regional seasonally varying ML depth, H , is as defined by
594 Thomson and Fine (2003) and Li et al. (2005) for nearby (35 km north-west
595 of Barkley Canyon) Line P Station 3. The ML is thick in winter and spring
596 (down to about -60 m), and thinnest summer through early-fall (up to about
597 -20 m). There are large wind data gaps during later years (2014, 2017, and
598 2018), so 2013 is used as the sample year. Results for later years are available
599 in Appendix A. Results yield time series of NI ML currents exceeding 0.1 m
600 s^{-1} that are qualitatively similar to wind data, most notably in the fall and
601 early-winter. However, not every event that shows up in the ML is evident in
602 the NI depth-band observations.

603 Seasonal slab model correlations (not shown) with NI depth-band power sug-
604 gest interior NI response to wind forcing is strongest in summer and fall.
605 Seasonal correlations were obtained similarly to diurnal spring-neap forcing.
606 The slab model does poorly on a short-term basis, but if binned over three
607 weeks the amount of energy input by the wind and found in the ADCP data
608 shows reasonable agreement. It is possible that the apparent delay in the deep

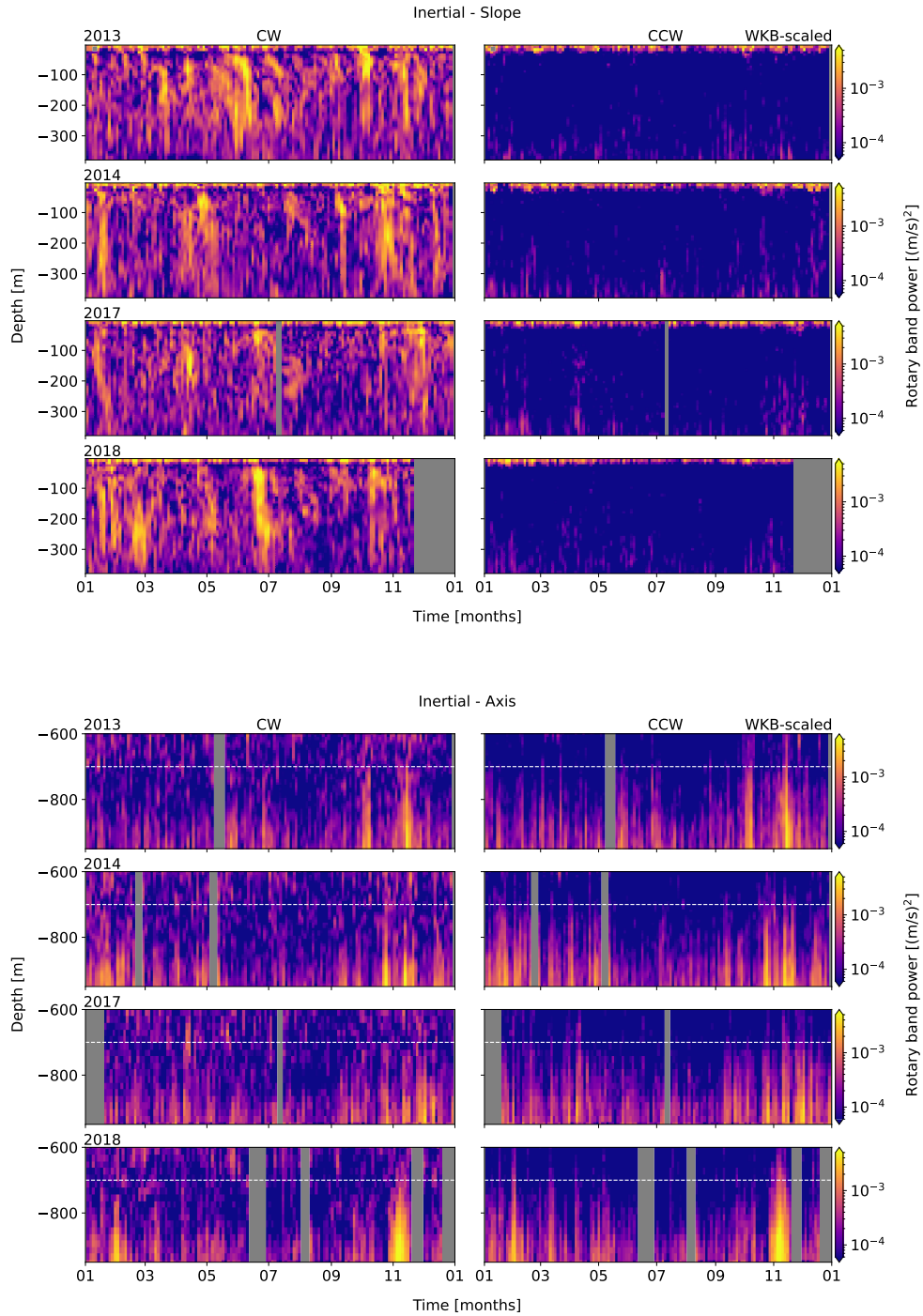


Figure 18. Band-integrated NI rotary PSD for SLOPE (upper) and AXIS (lower), from WKB-scaled horizontal velocity data. CW (left) and CCW (right) components are shown. Each row represents an analysis year, labelled at upper-left.

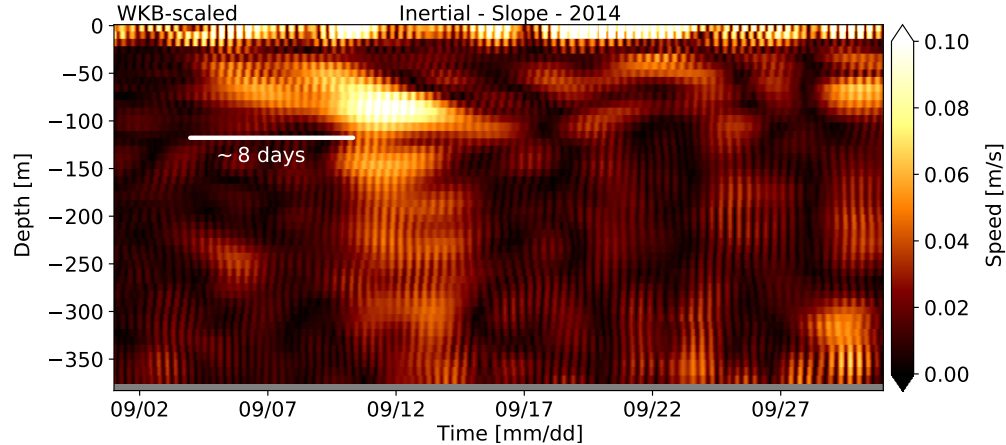


Figure 19. Transfer of NI energy in band-passed NI velocity (total) for September of 2014. A wind event excites NI energy in the ML around September 9. Energy is transferred down to about -100 m over about 8 days, after which there is a deep response.

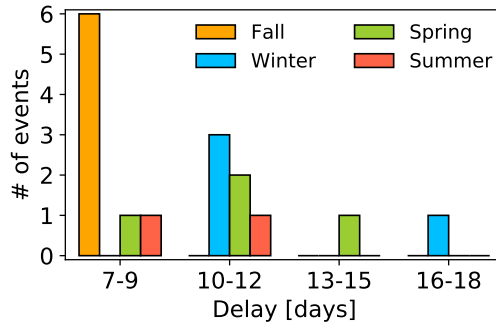


Figure 20. Histogram of delayed NI events. Delayed NI deep response events are most common and short-lived in the fall, least common in summer, and longest in the winter.

609 response may affect correlation with the relatively quickly influenced ML. At
 610 SLOPE, correlations are strong-positive in the fall, and medium-positive in
 611 summer. At AXIS, correlations are strong-positive in summer, and medium-
 612 positive in fall. Seasonal correlations are otherwise inconsistent, and may be
 613 further complicated by the location of the wind data buoy, 50 km north of
 614 Barkley Canyon. The fall and summer correlation periods encompass notable
 615 wind events that occur while the ML is thin and there is a more notable deep
 616 response.

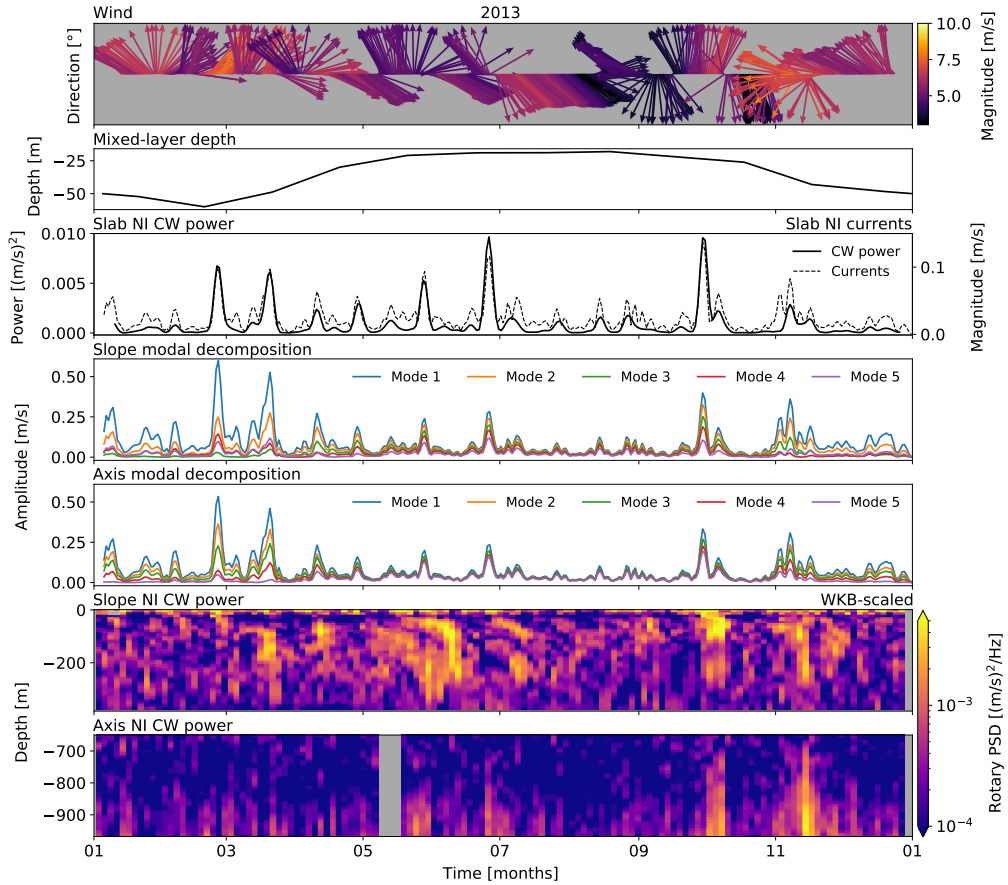


Figure 21. NI forcing analysis for 2013. From top to bottom: wind direction and amplitude; monthly-averaged ML depth for Line P station 3 as determined by Li et al. (2005); slab model NI CW power and NI currents; seasonal mode amplitudes for SLOPE and AXIS; and for reference, band-integrated NI CW power at SLOPE and AXIS. There appears to be a complex relationship between the wind, ML, slab currents, and mode amplitudes in driving the NI observations, with the most obvious effects in the fall. Due to significant data gaps, plots for other analysis years are in Appendix A.

617 Seasonal vertical mode amplitudes suggest high-mode contributions lead to
 618 greater NI deep response (Figure 21 - modal decompositions). For NI IW gen-
 619 eration by NI ML currents, the stratification-dependent vertical mode struc-
 620 ture is determined as described in Section 3. When the ML is thin, contribu-
 621 tions from low modes (1 and 2) and high modes (3, 4, 5) are about equal ($\sim 52\%$ low modes). When the ML is thick, modes 1 and 2 dominate ($\sim 74\%$).
 623 Similar to the slab correlations, there is a greater deep response when the ML
 624 is thin and higher modes are equal contributors, such as in the early-fall when

625 strong storms begin to arrive. High modes contribute most in the summer
626 when the ML is thinnest, though there are few storms this time of year. How-
627 ever, even the weak summer wind events occasionally warrant a deep response.
628 In contrast, there is often little or no deep response to the many strong wind
629 events in winter and spring when the ML is thick and low modes dominate. A
630 deep response associated with high-mode NI IW is not unexpected, as other
631 observations have shown a poor local response to low-mode forcing, with the
632 reasons poorly understood (Gill, 1984; Zervakis & Levine, 1995; Alford, 2003).
633 While low-modes appear to dominate NI IW energy they largely propagate lat-
634 erally, while high-mode energy radiates downward and equatorward (Alford et
635 al., 2016). It is likely that modal analysis is a poor model here, and that the
636 complex balance of up and down low- and high-mode energy makes identifying
637 forcing of the deep response difficult.

638 **5.2.4 Semidiurnal**

639 Semidiurnal ($2.17 - 2.39 \times 10^{-5}$ Hz) seasonality at SLOPE (Figure 22 - up-
640 per) is inter-annually consistent and subtle, showing a slight pulse that begins
641 in the late-spring/early-summer (months 4/5) and an even weaker pulse in
642 the fall/early-winter. Seasonality at AXIS (Figure 22 - lower) is not readily
643 apparent.

644 Semidiurnal barotropic spring-neap forcing is intermittently in-and-out of phase,
645 at both sites, suggesting some remote baroclinic forcing (Figure 23). Phase-lag
646 correlations were determined as for the diurnal band. The scaled semidiurnal
647 depth-mean band-power amplitudes vary greatly from the seasonal spring-
648 neap surface levels. Fortnightly phase-lags are inconsistent, and for 3-month
649 correlation periods range from 0 to 4 days at SLOPE (inter-annual average of
650 2.3 days), and from 0 to 6 days at AXIS (inter-annual average of 2.8 days). The
651 irregularity of the phase-offset suggests a mix of local barotropic and remote
652 baroclinic forcing.

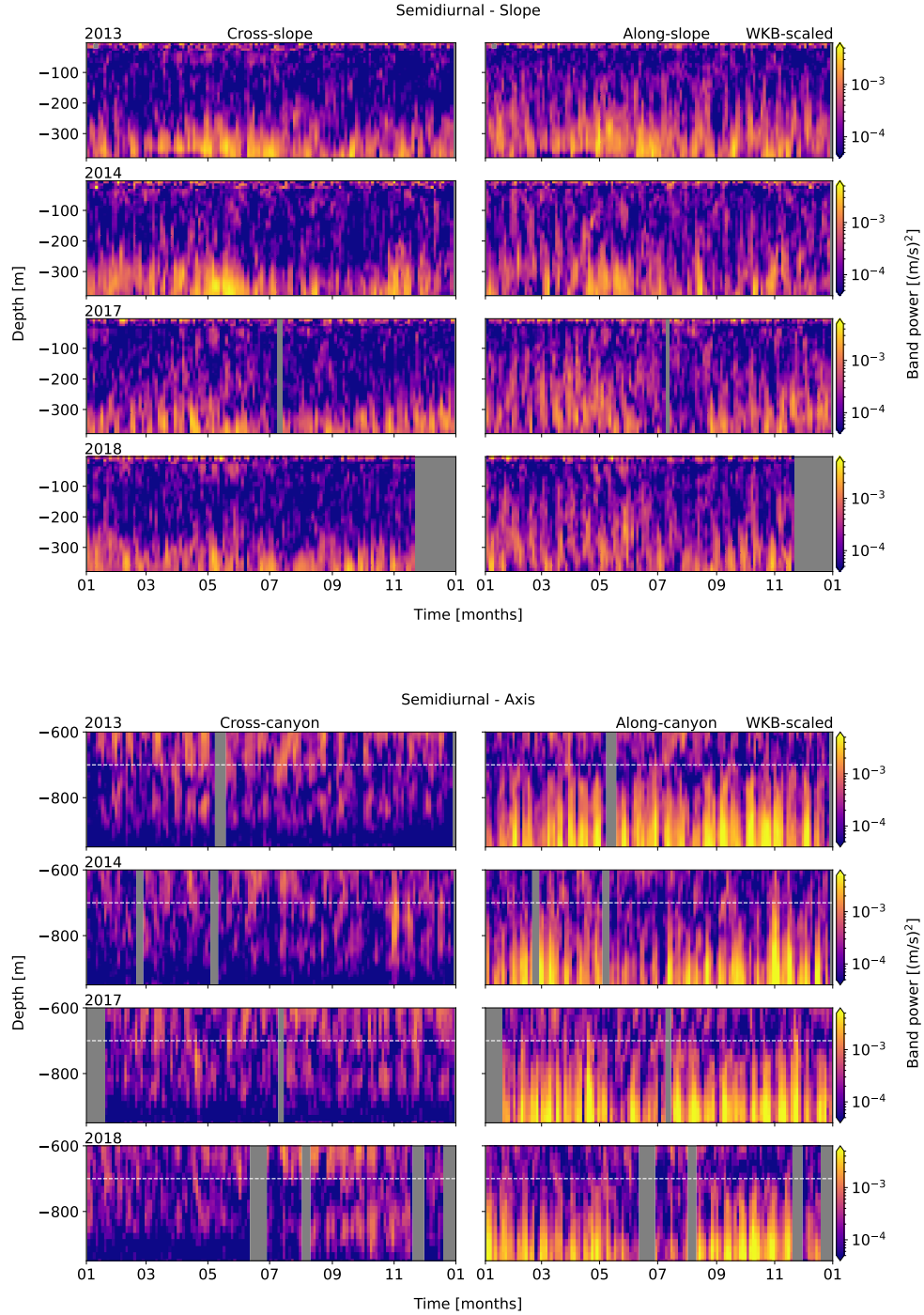


Figure 22. Band-integrated semidiurnal PSD for SLOPE (upper) and AXIS (lower), from WKB-scaled horizontal velocity data. Cross- (left) and along-slope/canyon (right) components are shown. Each row represents an analysis year, labelled at upper-left.

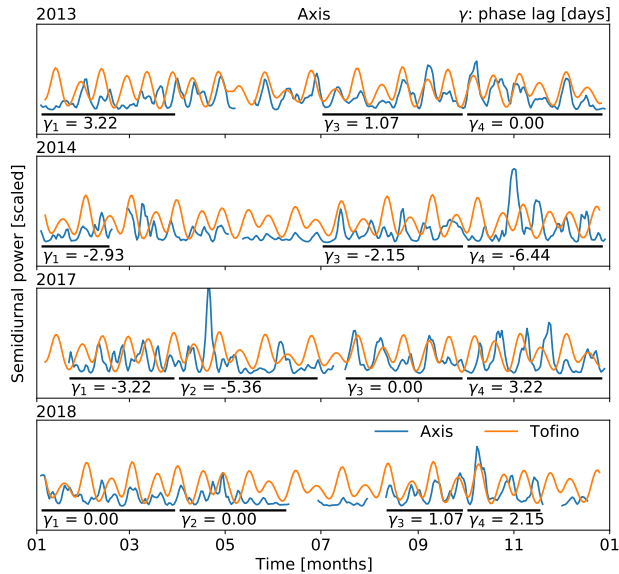
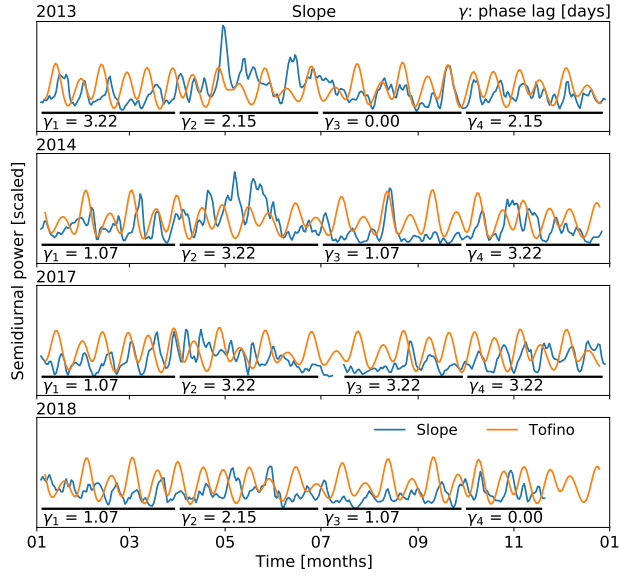


Figure 23. Semidiurnal barotropic forcing comparison. Phase and amplitude (scaled) comparisons for band-integrated power of semidiurnal surface level data (Tofino, orange) and WKB-scaled depth-mean semidiurnal power (blue) at SLOPE (top) and AXIS (bottom). Black bars indicate seasonal correlation ranges. Though the instrument amplitude is highly irregular, there is a variable phase lag that suggests a mix of local barotropic and remote baroclinic forcing.

653 **5.2.5 High-frequency internal wave continuum**

654 Variability of high-frequency IW continuum energy ($7.00 \times 10^{-5} - 1.20 \times 10^{-4}$
 655 Hz) at SLOPE (Figure 24 - upper) is inter-annually consistent, heightened in
 656 spring through early-summer, and again through the fall. At AXIS (Figure 24
 657 - lower), variability is less apparent, though there is generally greater energy
 658 in the fall.

659 At both sites, the observed high-frequency continuum amplitude is higher,
 660 and the spectral slope steeper, as compared to the open-ocean GM spectrum
 661 (Figure 25). For near-bottom depth-specific time series of WKB-scaled PSD
 662 (-300 m at SLOPE and -900 m at AXIS), a power law of af^b was fit to the high-
 663 frequency continuum band and smoothed in two week intervals, resulting in
 664 time series of power law amplitude (a) and slope (b). As the open-ocean GM
 665 spectrum can vary slightly depending on f and other parameters, a similar fit
 666 was applied to find $a_{GM,0.5} \approx 2.7 \times 10^{-9} \text{ m}^2 \text{ s}^{-2} \text{ Hz}^{-1}$ (its energy halved to
 667 compare with observed u and v components) and $b_{GM,0.5} \approx -2.1$. At both sites,
 668 observed a ranges within $2 - 5 \times 10^{-9} \text{ m}^2 \text{ s}^{-2} \text{ Hz}^{-1}$, and b within -2.0 – -2.3,
 669 similar but generally higher amplitude and steeper slope compared to open-
 670 ocean GM values. Time series of power law amplitude and slope are strongly
 671 correlated, each a rough copy of depth-mean high-frequency continuum depth-
 672 band power variability (not shown).

673 Elevated near-topography high-frequency continuum energy leads to enhanced
 674 dissipation rates, ε , at both sites (Figure 26). WKB-scaled high-frequency
 675 continuum energy was 'whitened' over the continuum frequency range - its
 676 power multiplied by f^2 - then averaged to find mean continuum energy, E_c , in
 677 depth and time. Determined similarly, a mean value of open-ocean GM energy
 678 was found to be $E_{GM} \approx 8.1 \times 10^{-9} \text{ m}^2 \text{ s}^{-2} \text{ Hz}$. The ratio of E_c/E_{GM} is up to
 679 $7 \times E_{GM}$ near topography, while away from topography E_c levels fall to equal
 680 or below that of E_{GM} (not shown). From IW interaction theory (Althaus et
 681 al., 2003), dissipation estimates were calculated from the WKB-scaled E_c fits
 682 as:

$$683 \quad \varepsilon = \varepsilon_0 \frac{N_0^2}{N_{GM}^2} \frac{\langle E_c^2 \rangle^2}{\langle E_{GM}^2 \rangle^2} f(R_\omega) \quad (22)$$

684 where $\varepsilon_0 = 4.1 \times 10^{-11} \text{ W kg}^{-1}$, $\langle E_c^2 \rangle^2 / \langle E_{GM}^2 \rangle^2$ is the measured ratio of high-
 685 frequency continuum energy to GM energy over the same frequency range, and
 686 the upper bound $f(R_\omega)$ is defined as:

$$687 \quad f(R_\omega) = \left(\frac{R_\omega + 1}{R_\omega} \right)^2 \left[\cosh^{-1} \left(\frac{N_0}{f} \right) + \frac{25 \cos^{-1}(f/N_0)}{\sqrt{R_\omega}} \right] \quad (23)$$

688 as an energy ratio defined by Sun and Kunze (1999), with $R_\omega = 2.13$ (Kunze

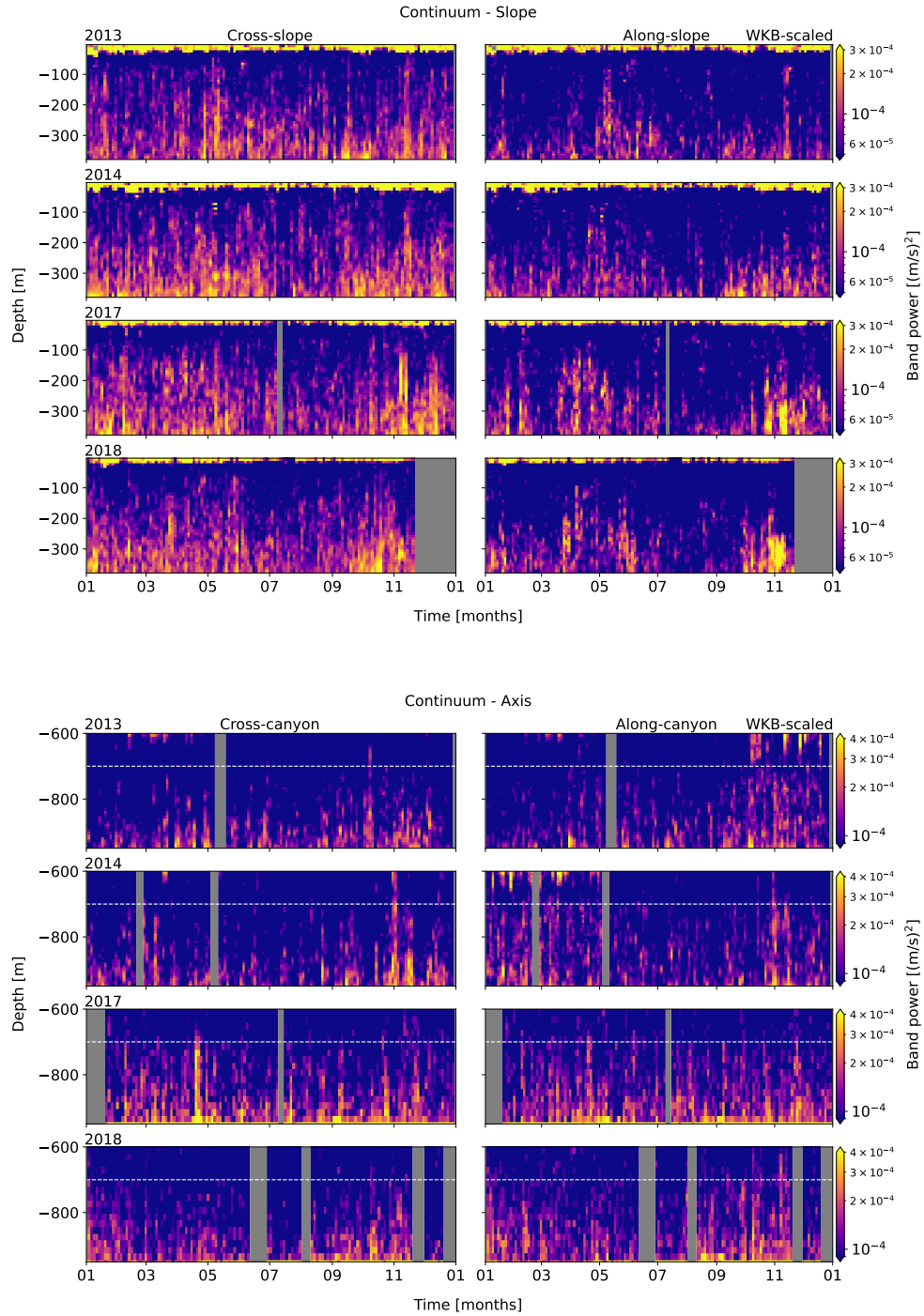


Figure 24. Band-integrated high-frequency continuum PSD for SLOPE (upper) and AXIS (lower), from WKB-scaled horizontal velocity data. Cross- (left) and along-slope/canyon (right) components are shown. Each row represents an analysis year, labelled at upper-left.

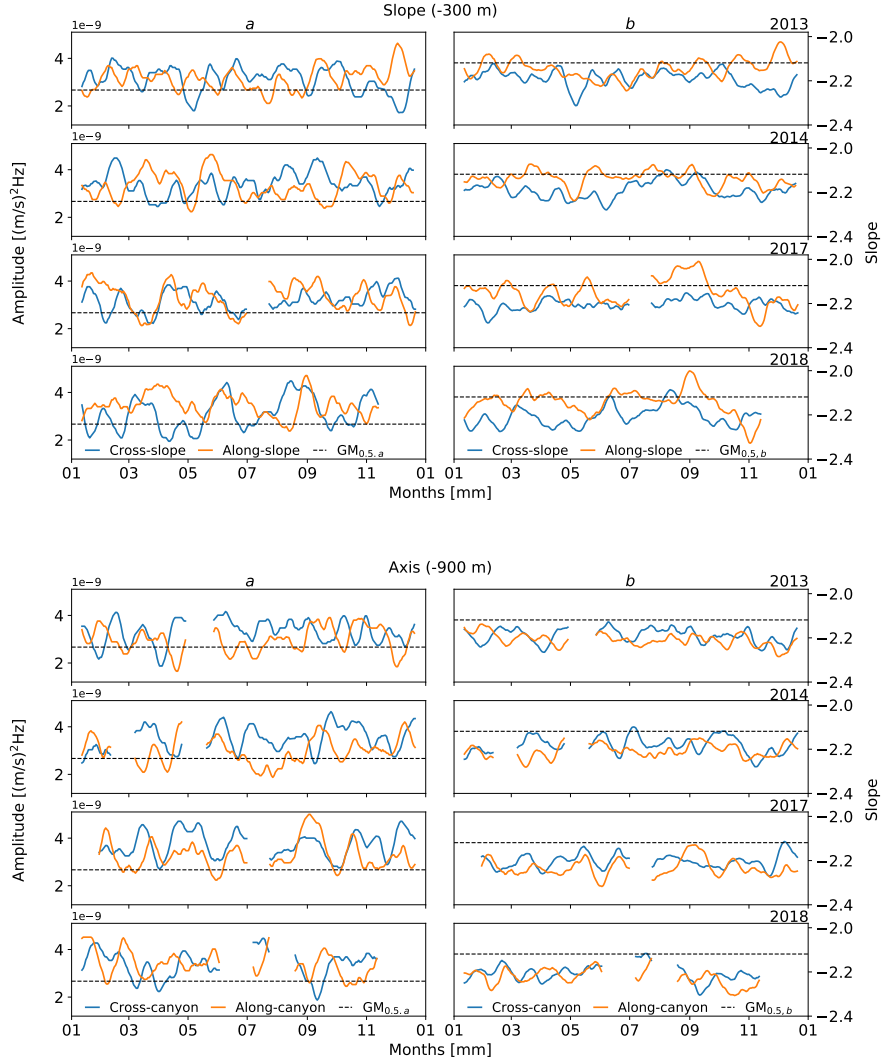


Figure 25. Time-series of high-frequency continuum power law fits. High-frequency continuum amplitude, a (left), and slope, b (right), of power law (af^b) fits to lower-depth WKB-scaled PSD, at SLOPE (top) and AXIS (bottom). For each site, each row is a year, labelled upper-right. Time series were smoothed over two weeks. Compared to GM, amplitudes are elevated up to $2\times$ GM in the centre of a near-bottom layer of elevated energy, with spectral slopes as negative as -2.3.

et al., 2002) for a high-frequency continuum with predominantly semidiurnal forcing (discussed in Section 6.4). Results reach 10^{-7} W kg $^{-1}$ near topography, fluctuating with high-frequency continuum energy variability. Away from topography, dissipation is on the order of 10^{-9} W kg $^{-1}$ or less. Turbulent eddy diffusivities, κ , are similarly elevated near topography (Figure 26). From

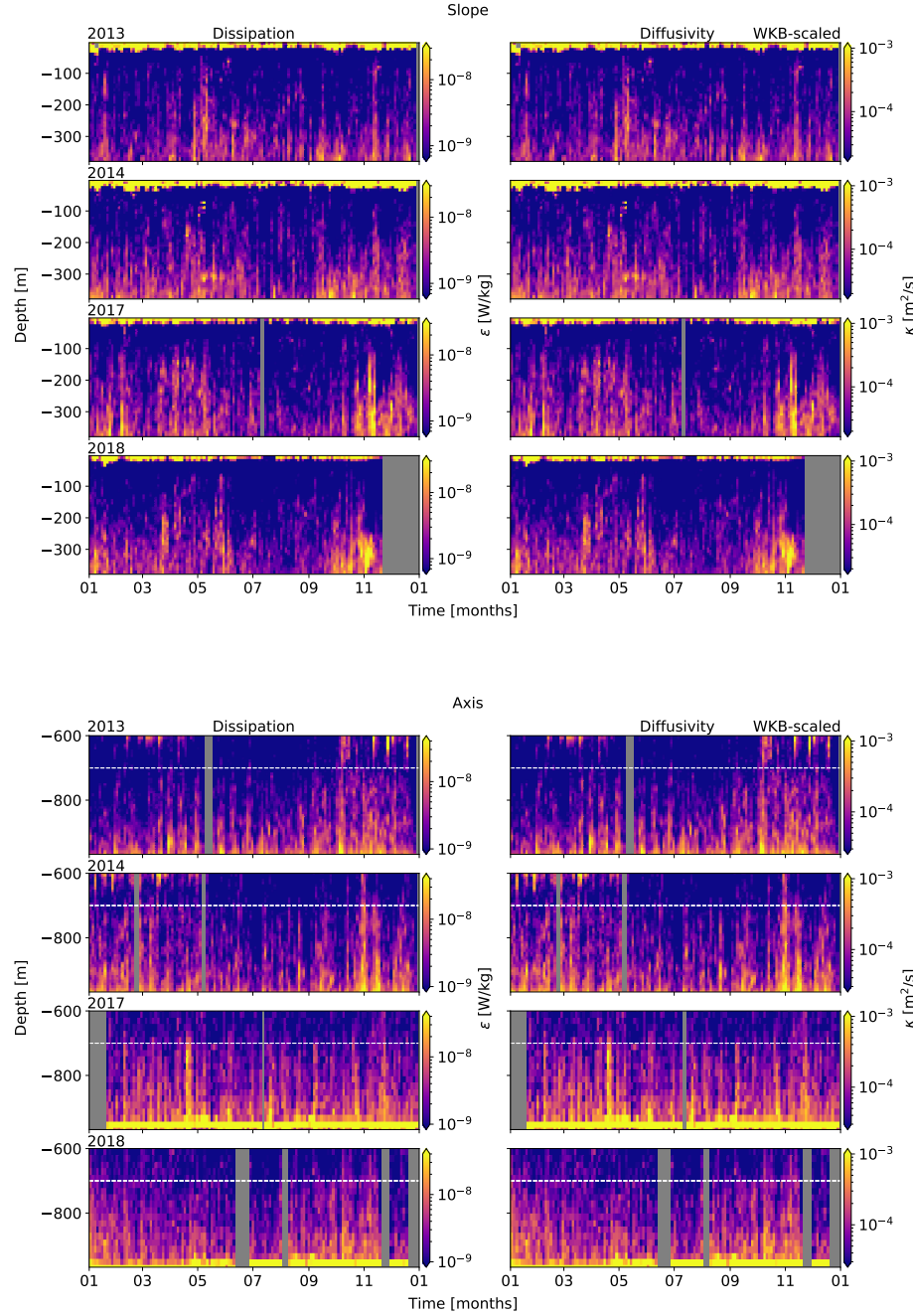


Figure 26. Dissipation rates (left) and turbulent eddy diffusivity (right), for WKB-scaled horizontal velocity spectra at SLOPE (top) and AXIS (bottom). Both dissipation and diffusivity are heightened near topography.

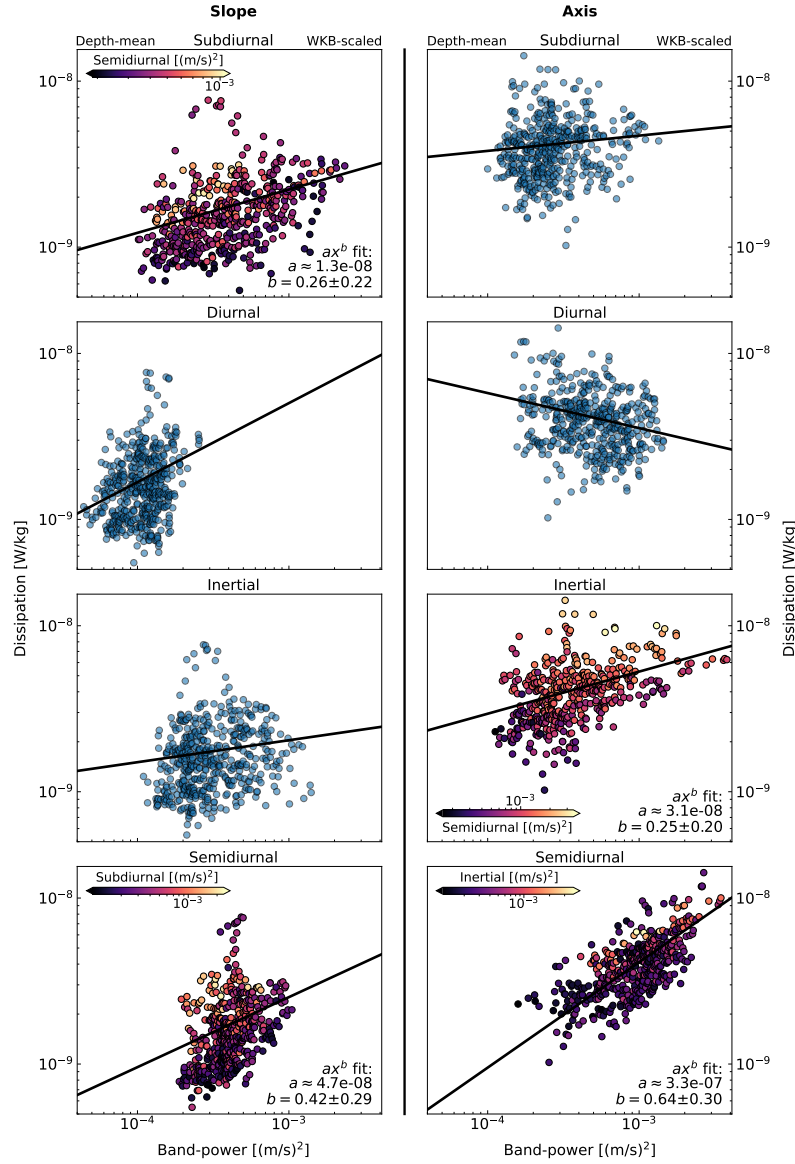


Figure 27. Dissipation power law fits. Scatter plots are for depth-mean WKB-scaled depth-band power at SLOPE (left) and AXIS (right), all years. Frequency constituents are listed for each row, as sub-diurnal (top), diurnal (second), NI (third), and semidiurnal (bottom). Black lines indicate the power law fit, listed in the lower-right of each frame. For each site, the two most likely contributors are coloured by the strength of the other.

694 ε , diffusivity was calculated as by Kunze et al. (2002), as:

$$695 \quad \kappa = \frac{\gamma \varepsilon}{N_0^2} \quad (24)$$

696 where $\gamma = 0.2$ is the mixing efficiency for high-Reynolds-number turbulence.
 697 Turbulent eddy diffusivities reach $10^{-3} \text{ m}^2 \text{ s}^{-1}$ near topography, again fluctuating
 698 with high-frequency continuum energy variability. Away from topography,
 699 diffusivity values are on the order of $10^{-5} \text{ m}^2 \text{ s}^{-1}$ or less, consistent with open-
 700 ocean values (Gregg, 1989; Kunze et al., 2002).

701 Dissipation variability (derived from high-frequency continuum energy vari-
 702 ability) is correlated with semidiurnal forcing at both sites (Figure 27), with
 703 secondary contributions from the sub-diurnal band at SLOPE, and the NI band
 704 at AXIS. Dissipation variability correlations were determined as for NI wind
 705 forcing, for each constituent (not shown). At SLOPE, the semidiurnal band
 706 shows moderate correlations throughout the year, and strong correlations in
 707 the spring, while the sub-diurnal band shows weak to moderate correlations in
 708 both winter and spring. At AXIS, the semidiurnal band is strongly correlated
 709 all year, while the NI band is moderate to strongly correlated in the spring and
 710 fall. There is no apparent fortnightly modulation of high-frequency continuum
 711 energy or vertical scales associated with diurnal or semidiurnal spring-neap ef-
 712 fects. To further quantify these relationships, power laws of ax^b were fit to
 713 scatter plots of depth-mean dissipation-power time series for each frequency
 714 constituent. The process was bootstrapped for improved uncertainties. At
 715 both sites the semidiurnal band shows the best fit, and is stronger at AXIS.
 716 Secondary contributors (the sub-diurnal band at SLOPE, and the NI band
 717 at AXIS) show less obvious fits. Both the semidiurnal and secondary bands
 718 contribute to higher dissipation as they increase, but they do not drive each
 719 other. The power law fits for semidiurnal driven dissipation are $\varepsilon \sim M_2^{0.42 \pm 0.29}$
 720 at SLOPE, and $\varepsilon \sim M_2^{0.64 \pm 0.30}$ at AXIS.

721 Multivariate analysis improves power law fits, reinforcing the importance of the
 722 secondary contributing constituents (Figure 28). Secondary constituents were
 723 added to the semidiurnal power law fits as $ax_1^b + cx_2^d$, where x_1 is the depth-
 724 mean semidiurnal band-power and x_2 is the secondary contributing band -
 725 sub-diurnal (Sub K_1) at SLOPE, and NI at AXIS. The process was again boot-
 726 strapped for improved uncertainties. Multivariate power law relationships of
 727 $\varepsilon \sim M_2^{0.83 \pm 0.17} + \text{Sub}_{K1}^{0.59 \pm 0.13}$ and $\varepsilon \sim M_2^{1.47 \pm 0.48} + \text{NI}^{0.24 \pm 0.06}$ were found for
 728 SLOPE and AXIS, respectively. At SLOPE, the purely semidiurnal fits are gen-
 729 erally overestimated, and conservative in periods of high and low dissipation,
 730 while multivariate fits are less conservative and better reflect seasonal variabil-
 731 ity. At AXIS, purely semidiurnal fits are reasonable, but generally underesti-

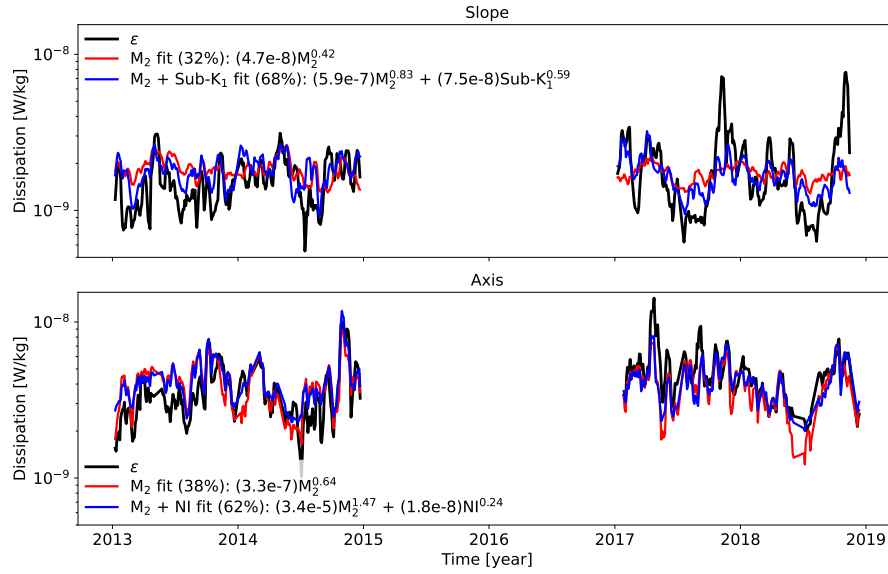


Figure 28. Dissipation multivariate power law fits for SLOPE (top) and AXIS (bottom). Shown are comparison time series of depth-mean WKB-scaled dissipation (black), semidiurnal power law fits (red), and multivariate power law fits (blue). Percent good is listed for each fit, as a measure of which fit line is closest to ε at each time step. Dissipation (black) time-series shows a seasonal trend towards a summer lull, with more energetic fall events in later years. The purely semidiurnal fits (red) are conservative in estimating periods of high and low energy at SLOPE, and often underestimate at AXIS. The multivariate fits (blue) are improved, less conservative in estimating extremes at SLOPE, and fairly accurate at AXIS.

732 mate dissipation in 2017 and 2018, while multivariate fits are fairly accurate
 733 in all years. A percent-good metric indicates the multivariate fits are better
 734 than univariate for 68% of data points at SLOPE, and 62% at AXIS.

735 5.2.6 Near- N

736 The build-up of energy at frequencies close to N (here defined between $2.00 \times 10^{-4} - 1.00 \times 10^{-3}$ Hz) is known as the near- N spectral 'shoulder' (Leder,
 737 2002). This feature was noted by Sabinin in 1966, and only occasionally in the
 738 time since (Pinkel, 1975; Kase and Clarke, 1978; Leder, 2002; D'Asaro et al.,
 739 2007; Pinkel, 2014; Alford, 2016), as it is typically unresolved in oceanographic
 740 power spectra. The 15-minute data used in this study only partly expose this
 741 feature. To properly analyse the shoulder, 2-second data from the 75 kHz RDI
 742 instruments were obtained to allow for increased Nyquist frequency. The data
 743 for this high-frequency range were then processed similarly to the lower fre-
 744 quency constituents. Shoulder depth-band power is elevated near topography,
 745 though less uniformly than for lower frequency constituents (Figure 29). At
 746

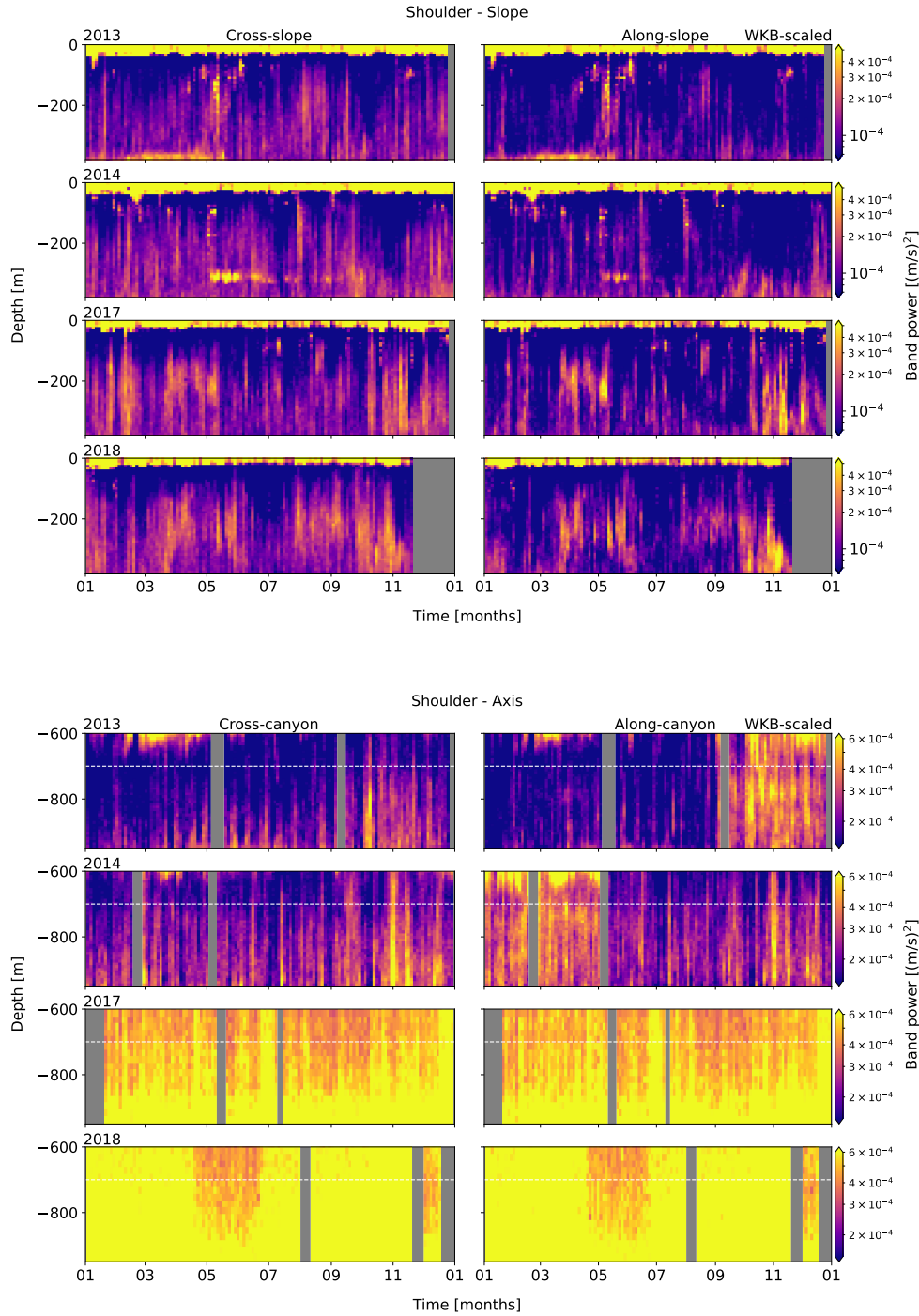


Figure 29. Band-integrated shoulder PSD for SLOPE (upper) and AXIS (lower), from WKB-scaled horizontal velocity data. Cross- (left) and along-slope/canyon (right) components are shown. Each row represents an analysis year, labelled at upper-left.

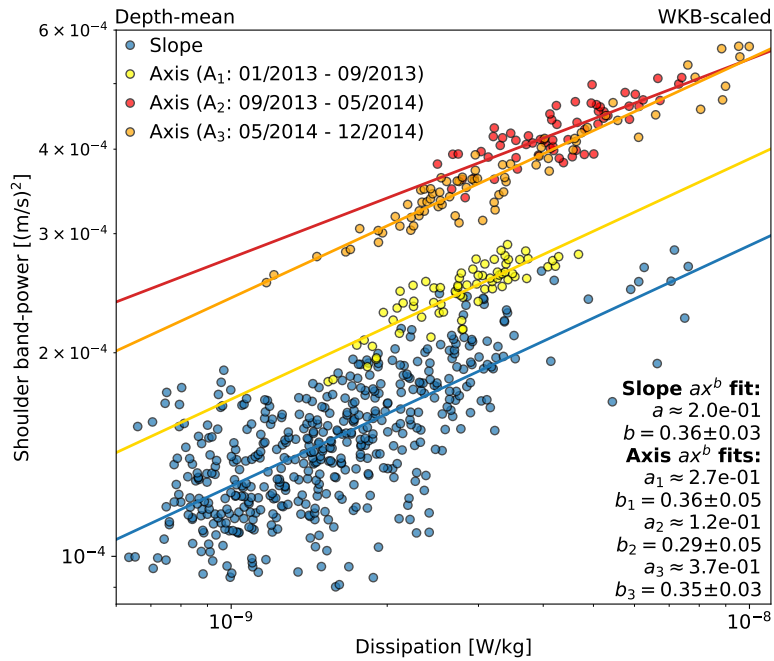


Figure 30. Power law relationship between dissipation and the spectral shoulder. Inter-annual depth-mean scatter plot for WKB-scaled dissipation and shoulder depth-band power, for SLOPE (blue) and AXIS (yellow, red, orange). SLOPE data is for all four analysis years. AXIS data is separated into three variance periods determined by instrument swaps and adjustments, for 2013 and 2014. All power law slopes agree within uncertainty, suggesting strong correlation to turbulence that does not depend on site topography.

747 SLOPE, shoulder power is mostly cross-slope and rectilinear, and somewhat
 748 intermittent in its depth-dependent enhancement. At AXIS, shoulder power is
 749 isotropic, and its depth-dependent enhancement more vertically uniform than
 750 at SLOPE. Shoulder power variability at SLOPE is subtle, somewhat heightened
 751 in the spring and fall, with intermittent brief pulses that are inconsistent in
 752 both depth and time. At AXIS, there is subtly increased energy in the fall.
 753 However, there are multiple issues with interpreting shoulder energy variabil-
 754 ity at AXIS. During 2013 and 2014, there were adjustments to ADCP beam
 755 orientation (2013/05 and 2014/05) relative to canyon topography, an instru-
 756 ment swap (2014/05), and a switch from 4- to 3-beam solutions (2013/05),
 757 somehow resulting in distinct periods of higher variance (though this did not
 758 affect lower frequencies, likely due to their broader horizontal scale). These
 759 periods are defined as A₁, A₂, and A₃. A₁ is 2013/01 - 2013/09, while the
 760 first RDI 75 kHz instrument was operating with a 4-beam solution. A₂ is

761 2013/09 - 2014/05, after the same instrument was adjusted to a 3-beam solu-
762 tion, showing heightened variance up to $3 \times A_1$. A_3 is 2014/05 - 2014/12, after
763 a new 75 kHz 3-beam instrument was swapped in, and variance was lowered
764 to up to $2 \times A_1$. It is possible that the difference between A_2 and A_3 could
765 be physical, as there is a coinciding drop in high-frequency continuum energy.
766 This is possible only if high-frequency continuum energy is not (or at least not
767 as much) affected by the instrument adjustments, which seems to be indicated
768 in the comparative variance of raw spectra. When an orientation adjustment
769 coincided with a variance jump (as in 2014/05), the rotation was minimal (up
770 to $\sim 20^\circ$), suggesting the wave field would have to be quite asymmetric to re-
771 sult in such a difference, which is unlikely. In 2017 and 2018, use of Nortek
772 55 kHz instruments at AXIS does not allow for clear resolution of the spectral
773 shoulder, as those instruments' noise floors are higher than that of the previ-
774 ous Teledyne RDI 75 kHz ADCPs (Figure 13). Re-evaluation of the spectral
775 shoulder variance at AXIS is worthwhile, but beyond the scope of this study.

776 There is a distinct power law relationship between turbulent dissipation (and
777 therefore high-frequency continuum variability) and the spectral shoulder (Fig-
778 ure 30). Power law fits for WKB-scaled depth-mean dissipation and shoul-
779 der depth-band power (P_{Sh}) were determined as for the high-frequency con-
780 tinuum analysis of Section 5.2.5. At SLOPE, there is a reasonable fit of
781 $P_{Sh_SLOPE} \sim \varepsilon^{0.36 \pm 0.03}$ for all four years. At AXIS, a power law was fit to
782 each of the three variance periods in 2013 and 2014. Though amplitudes
783 vary between periods, power law slopes are similar, with $P_{Sh_A_1} \sim \varepsilon^{0.36 \pm 0.05}$,
784 $P_{Sh_A_2} \sim \varepsilon^{0.29 \pm 0.05}$, and $P_{Sh_A_3} \sim \varepsilon^{0.35 \pm 0.03}$. Power law slopes at both SLOPE
785 and AXIS all agree within uncertainty (averaging $P_{Sh} \sim \varepsilon^{0.34 \pm 0.08}$), suggest-
786 ing a connection between spectral shoulder energy and turbulence that does
787 not depend on site topography. The shoulder appears to vary weakly with
788 high-frequency continuum energy, perhaps not responding as quickly to the
789 external forcing because of the time it takes for energy to cascade from low to
790 high wave frequencies.

791 6 Discussion

792 6.1 Canyon axis mean currents

793 The periodic (\sim week) up-canyon mean flow at AXIS (between -700 and -900
794 m), with its underlying near-bottom down-canyon layer, is notable for its sea-
795 sonal and inter-annual consistency and circulation implications (close to zero
796 net mean flow), important for understanding sediment transport and physical-
797 biological coupling influencing VICS productivity (Xu & Noble, 2009). In pre-

798 vious biological studies at Barkley Canyon (Cabrera et. al, 2018; Chauvet et
799 al., 2018), a two-layer flow system was noted similar to that of both Hudson
800 Canyon (Hotchkiss & Wunsch, 1982) and Monterey Canyon (Xu & Noble,
801 2009). These systems were attributed to circulation cells caused by along-
802 canyon pressure gradients driven by consistent large-scale quasi-geostrophic
803 along-shelf regional currents, similar to those observed at SLOPE. The up-
804 ward propagation of these currents was observed with periodicity ranging from
805 semidiurnal at Monterey Canyon, to $>$ than a few days at Hudson Canyon, and
806 found to shoal at an angle similar to that of the up-slope gradient (Hotchkiss
807 & Wunsch, 1982; Petruncio et al., 1998; Xu & Noble, 2009). Tidal rectifica-
808 tion, where tides force an up-slope pressure gradient (Garrett, 2004), could
809 also drive a periodic mean up-canyon flow. The associated near-bottom ($<$
810 50 m) down-canyon flow could be linked to turbidity currents and river-flood-
811 induced underflows, that occur as shelf sediment descends through canyons
812 to the ocean interior (Xu & Noble, 2009; Chauvet et al., 2018). At Barkley
813 Canyon, where large-scale regional mean currents move consistently along-
814 slope across the mouth and rim of the canyon, this seems a likely explanation.
815 However, tidal rectification and turbidity currents cannot be ruled out.

816 To associate the observed AXIS mean flow with these potential forcing mech-
817 anisms, correlations were computed for the observed along-canyon periodic-
818 ity and mean currents at SLOPE, fortnightly spring-neap tidal influence, and
819 depth-mean semidiurnal depth-band power. Correlations are inconsistent (not
820 shown), and do not suggest forcing by these sources. However, though there is
821 no obvious connection to diurnal or semidiurnal spring-neap forcing, estimates
822 of total lower-canyon transport (below -700 m) from depth- and time-mean an-
823 nual velocities result in near-zero net up-canyon flow (annually between 0.004
824 - 0.005 m s^{-1}), potentially consistent with tidal rectification theory.

825 Though along-canyon mean flow systems have been noted at other canyons,
826 the periodicity and attributed forcing comparisons at Barkley Canyon do not
827 align with other studies, as there is little correlation to SLOPE mean currents,
828 the spring-neap cycle, or semidiurnal energy. It seems most likely that this
829 circulation is driven by the strong regional mean currents that exist at SLOPE,
830 though tidal rectification and turbidity currents may contribute. It is possible
831 that such circulation may be common in shelf-incising canyons, but that forcing
832 is dependent on unique site characteristics and regional physical processes, and
833 so is difficult to determine. Further evaluation is necessary, and beyond the
834 scope of this study.

835 6.2 Tidal currents

836 The diurnal and semidiurnal tidal constituents are two of the greatest sources
837 of IW energy, and affect mean currents, mixing, IT and baroclinic shelf wave
838 propagation, and VICS circulation and productivity (Crawford & Thomson,
839 1984; Cummins & Oey, 1997).

840 For the diurnal constituent, there is elevated energy in the late-spring and sum-
841 mer. Results are consistent with previous studies in the region. Drakopolous
842 and Marsden (1993) associated strengthened diurnal tidal flow over the VICS
843 with increased stratification in summer, while Cummins et al. (2000) sug-
844 gest diurnal currents are seasonally responsive to the large-scale spring shift
845 to equatorward, upwelling-favourable mean currents. Xu and Noble (2009)
846 found inter-annually consistent K_1 currents in Monterey Canyon that peaked
847 relative to the annual cycle of spring-neap tidal forcing, as observed here.

848 As the diurnal (and sub-diurnal) frequency is sub-inertial, diurnal IT are
849 evanescent (trapped) to topography north of their turning latitude ($\sim 30^\circ\text{N}$),
850 unable to radiate offshore. Cummins and Oey (1997) found that trapped di-
851 urnal IT generation was prevalent on the VICS adjacent continental slope,
852 similar to other Pacific slopes (Rudnick et al., 2015) and seamounts (Robert-
853 son et al., 2017). It is unlikely for there to be incident baroclinic diurnal IW
854 or IT unless they propagate along the shelf. However, if a diurnal spring-neap
855 phase-lag of up to a day is present, as potentially observed at SLOPE, this
856 suggests a remote baroclinic generation site within about 200 km, based on
857 a K_1 mode-1 wave speed of about $c_1 \sim 2.0 \text{ m s}^{-1}$ (Crawford & Thomson,
858 1984). One candidate would be diurnal shelf waves generated by oscillatory
859 tidal currents near the mouth of the Juan de Fuca Strait ($\sim 100 \text{ km}$ east
860 of Barkley Canyon) that propagate poleward along the VICS (Crawford &
861 Thomson, 1984; Flather, 1988). Confirmation of such waves would require
862 additional instruments along the shelf, and is beyond the scope of this study.
863 Other regions thought to be productive for baroclinic diurnal waves are either
864 disconnected from the shelf (e.g. the abyssal Juan de Fuca Ridge) and can-
865 not propagate sub-inertially to Barkley Canyon (Lavelle & Cannon, 2001), or
866 too distant for the observed phase-lag (e.g. Mendocino Escarpment, 900 km
867 south of Barkley Canyon; Morozov, 2018). As there is enough uncertainty in
868 the correlations that the phase-lag could effectively be null, and considering
869 the vertically linear structure present, it is likely that the diurnal band is pri-
870 marily forced by the local barotropic spring-neap cycle, with possible seasonal
871 contributions from shelf-waves, mean current interactions, or stratification.

872 In contrast, the semidiurnal constituent is locally super-inertial, able to freely
873 propagate away from topography as IT. There could be incident remote semidi-

iurnal IT at Barkley Canyon, contributing to the highly variable response. For
874 a semidiurnal phase-lag up to four days, as potentially observed at SLOPE, a
875 regional mode-1 M_2 phase speed of $c_1 \sim 3.0 \text{ m s}^{-1}$ (Zhao et al., 2016) suggests
876 a baroclinic generation site up to 1000 km away. A likely candidate is the
877 Mendocino Escarpment running east-west off of Northern California, one of
878 the strongest generation sites for low-mode semidiurnal IT in the northeast
879 Pacific (Althaus et al., 2003; Arbic et al., 2012; Zhao et al., 2017; Morozov,
880 2018). Strong tide-topography generated northward propagating mode-1 M_2
881 IT, along with the escarpment's location about 800 km due south of Barkley
882 Canyon (~ 3.5 days), agree reasonably with the observed phase lag. Other
883 potential semidiurnal IT generation sites are closer (e.g. the mouth of Juan
884 de Fuca Strait ~ 100 km, or the abyssal Juan de Fuca Ridge ~ 400 km), or are
885 somewhat obstructed by land (e.g. the Haida Gwaii Islands to the north), but
886 could contribute.

887 Furthermore, for free incident semidiurnal IT, the criticality of the impacted
888 topography can lead to focusing, breaking, or reflection, contributing to the
889 elevated near-topography turbulent layers observed. Barkley Canyon is gener-
890 ally supercritical or near-critical to incident semidiurnal IT (Figure 4). Critical
891 slope regions were determined from the gradient of bathymetric data obtained
892 from the National Oceanic and Atmospheric Administration (NOAA) National
893 Centre for Environmental Information, as 3 arc-second resolution mean sea
894 level depth. At the SLOPE mooring, the local slope is $\beta \approx 0.060$, supercritical
895 to the semidiurnal propagation angle $\alpha_{M2} \approx 0.026$ at that depth (Figure 5).
896 This suggests downward reflection (CW) and focusing of incident semidiurnal
897 IT, as observed. The SLOPE mooring sits adjacent to a large near-critical region
898 below the shelf-break (Figure 4), which, along with the VICS itself, is another
899 source of observed downward semidiurnal energy (Drakopoulos & Marsden,
900 1993). At other slope sites, there is evidence of elevated near-bottom energy-
901 flux associated with both semidiurnal IT generation and incident reflection,
902 with similar vertical scales within a few hundred metres above bottom (Terker
903 et al., 2014; Xie & Chen, 2021). For the AXIS mooring on the canyon floor,
904 local criticality is $\beta \approx 0.019 < \alpha_{M2} \approx 0.036$ (Figure 5). As such, this portion
905 of the canyon floor is subcritical to semidiurnal IT, suggesting upward reflec-
906 tion (CCW). However, as the canyon walls are generally supercritical, and the
907 surrounding floor is near-critical (Figure 4), the propagation of semidiurnal IT
908 at AXIS is likely complex. Xu and Noble (2009) found that deep in Monterey
909 Canyon semidiurnal IT were not only scattered up-canyon along the subcrit-
910 ical floor, but also reflected down by the supercritical walls, highly focusing
911 semidiurnal energy near the bottom. The potential for scattering, reflection,
912 focusing, and generation of semidiurnal IT all near the AXIS mooring could

914 lead to the observed highly 'channeled' deep-canyon semidiurnal response.
915 Together, the irregular nature of the semidiurnal spring-neap phase-lag and the
916 potential for critical IT-topography interactions suggests that forcing is a mix
917 of local barotropic and incident IT. As the barotropic tide passes over Barkley
918 Canyon, near-critical slope topography generates and focuses semidiurnal IT,
919 which radiate downward from the shelf-break to the slope and canyon, where
920 further downward reflection and focusing occurs. Remote incident IT are also
921 subject to these effects, and alter observed spring-neap phase based on their
922 origin, likely Mendocino Escarpment to the south. Finally, as the little annual
923 seasonality in the local barotropic spring-neap forcing cannot explain large-
924 scale inter-annual features in the observations, such as the subtle yet consistent
925 spring increase in semidiurnal energy at SLOPE, secondary contributors may
926 include seasonal changes to stratification (Drakopoulos & Marsden, 1993) and
927 mean currents (Cummins et al., 2000).

928 6.3 Near-inertial forcing

929 NI IW generated by wind events are thought to be significant contributors to
930 mixing in the deep ocean, of similar magnitude to the conversion of barotropic
931 tide to baroclinic internal tide energy (Alford et al., 2012). As such effec-
932 tive contributors to deep ocean energy, it is interesting that associated NI
933 energy can be so strongly attenuated with depth at SLOPE, while still eliciting
934 a deep response at AXIS. The timing of these events is qualitatively linked,
935 so the difference in topography likely modulates the response. Thomson et
936 al. (1990) found that NI IW become increasingly attenuated as they approach
937 slopes, absorbed by strong vertical shear in the background flow associated
938 with topographically trapped oscillations. Yet observed NI IW energy is en-
939 hanced near the canyon floor, not attenuated. Alford et al. (2016) note that
940 canyon walls confine the typically circular motion of NI waves, forcing them
941 rectilinearly along-canyon.

942 It may be that canyon topography uniquely effects the modal structure of ML
943 generated NI waves. Mode-1 amplitudes up to 0.6 m s^{-1} occur after notable
944 wind events, and while low modes generally dominate, more NI activity is ob-
945 served when the ML is thin and high modes are prevalent, similar to findings
946 by Jarosz et al. (2007) in DeSoto Canyon. Alford et al. (2016) note that high
947 mode waves propagate downward and equatorward, while low mode waves
948 contribute more to lateral propagation of NI energy. Ultimately, the down-
949 ward propagation of NI IW is difficult to characterise, as there are so many
950 factors to consider, including topography, seasonal thermocline thickness, β -
951 plane effects, and near-surface mesoscale vorticity adjusting local f_0 (Alford

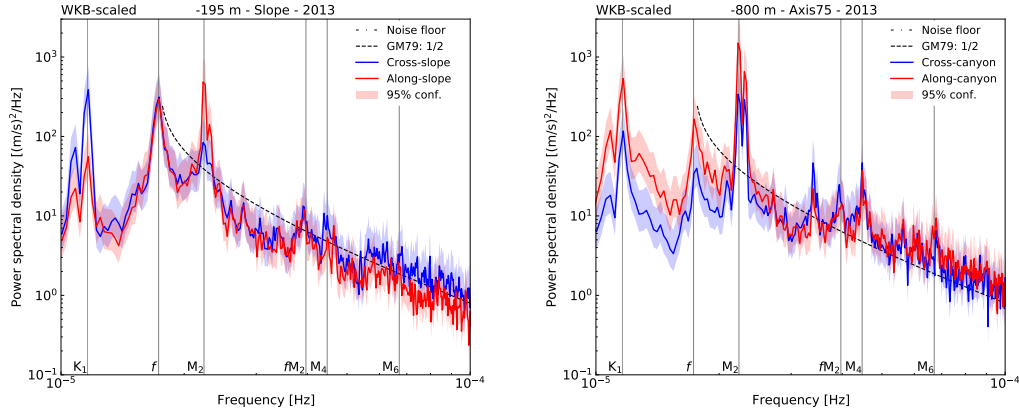


Figure 31. High frequency-resolution mid-depth PSD of WKB-scaled horizontal velocity data, for SLOPE (left) and AXIS (right), in 2013. Frequency scale is zoomed to the tidal range. There are no additional peaks or apparent blue-shift for the NI constituent, suggesting local forcing.

et al., 2016). Potential secondary forcing could be mean currents or lee waves of NI frequency across the mouth or rim of the canyon, where topographic attenuation of downward NI energy may be reduced due to the relative openness of those areas, driving deep along-canyon NI currents.

Regarding the delayed NI deep response to wind events, D'Asaro (1995) made a similar observation of an 8-10 day event, and theorised that divergence-forced NI pumping at the ML base causes oscillating pressure gradients in the thermocline, accelerating NI currents at depth. The rate of vertical energy transfer depends on the horizontal scale of the ML NI currents, with smaller horizontal scale ML currents propagating vertical energy faster. As vertical modes have progressively slower horizontal group velocities, the low modes propagate their energy away, first. As the low mode energy propagates away, the available energy and horizontal scale of the ML inertial currents decreases. Vertical energy propagation into the thermocline increases accordingly, with a notable maximum associated with a timescale of the departure of modes 1 and 2 (up to 10-20 days), described as 'inertial beating', after which the deep response rapidly increases and NI energy is evenly distributed between the upper thermocline and lower depths (Gill, 1984; D'Asaro, 1995; Zervakis & Levine, 1995).

The results suggest that local NI forcing is complex, dependent on variable characteristics of both wind events and ML processes, leading to highly intermittent seasonality in the interior. Remote forcing is also possible, as free NI

974 IW generated at the base of the surface mixed-layer must propagate equator-
975 ward due to the effects of turning latitudes (Alford et al., 2016). There is often
976 a blue-shift of the f spectral peak associated with remote NI forcing (Garratt,
977 1977; Voelker et al., 2020). However, high frequency-resolution spectra (Fig-
978 ure 31) do not resolve any additional NI peaks. Regardless, strong qualitative
979 and moderate quantitative correlations suggest that the NI observations are
980 most responsive to wind events when the ML is thin and high-mode contri-
981 butions are prevalent, particularly in the late-summer and fall. To summarise
982 the efficacy of attempting to characterise vertical NI processes, Alford et al.
983 (2016), when discussing the foundational Ocean Storms Experiment (D'Asaro,
984 1995), stated that “neither the decay of mixed-layer motions nor the rate of
985 energy transfer into the deep ocean can adequately be predicted for the best-
986 documented storm response on record”. Needless to say, additional research
987 is necessary.

988 6.4 Continuum-dissipation estimates

989 Topographic focusing of low-frequency IW and IT enhances energy, elevating
990 the high-frequency continuum amplitude and driving mixing (Polzin, 2004).
991 This is indicated by the heightened amplitudes and steep spectral slopes of
992 the observed high-frequency continuum, as compared to open-ocean GM val-
993 ues (Figure 25). As IW energy cascades from low- (tidal and sub-inertial)
994 to high-frequency processes, continuum energy variability should reflect this
995 transfer (Polzin, 2004). At both sites, high-frequency continuum energy vari-
996 ability correlations and power law fits indicate the semidiurnal constituent is
997 the greatest contributor to dissipation. Secondary contributors are the sub-
998 diurnal band at SLOPE, and NI band at AXIS. There are likely lesser contrib-
999 utions from other constituents. For continental slopes, mean currents and
1000 semidiurnal IT have both been noted to contribute to increased near-bottom
1001 dissipation rates (Nash et al., 2007; Kunze et al., 2012), as observed here.
1002 Similarly, in submarine canyons, the semidiurnal constituent has been found
1003 to be the primary contributor to seasonal, near-bottom mixing (Kunze et al.,
1004 2002; Waterhouse et al., 2017). However, there is a lack of evidence for the
1005 observed deep-canyon NI IW energy, as discussed in Section 6.3. Also evident
1006 is the non-isotropic nature of the high-frequency continuum, in contrast to a
1007 theoretical GM open-ocean IW field, though this departure from theory is not
1008 surprising considering the strong topographic guiding of flow.

1009 Winding canyons are hot spots for turbulence, as the reflection of IW at rough
1010 topography generates dissipation and scattering (Thorpe, 2001). Near topog-
1011 raphy in Monterey Canyon, Kunze et al. (2002) found spring-neap dependent
1012 average turbulent dissipation rates from 10^{-9} to $10^{-6} \text{ W kg}^{-1}$ and diffusivity

from 10^{-6} to $10^{-2} \text{ m}^2 \text{ s}^{-1}$, respectively, consistent with other studies (Carter & Gregg, 2002) and similar to those observed here ($\varepsilon \sim 10^{-8} \text{ W kg}^{-1}$ and $\kappa \sim 10^{-5} \text{ m}^2 \text{ s}^{-1}$). Carter and Gregg (2002) used observed values from Monterey Canyon for stratified turbulent layer thickness ($\sim 135 \text{ m}$), ε ($1.36 \times 10^{-6} \text{ W kg}^{-1}$), and global approximations of shelf length occupied by canyons (15,500 km) and canyon length (20 km) to estimate global dissipation in canyons as roughly 56 GW, or 16% of global internal tide dissipation. Using this method and ε observations from the lower extent of the AXIS turbulent layer ($\varepsilon \sim 10^{-7} \text{ W kg}^{-1}$) results in an estimate of only 4 GW of global dissipation in canyons, or 1% of global internal tide dissipation. This disparity indicates that individual canyon topography strongly affects dissipation rates, and assumptions for global mixing budgets require further constraints. However, the observations by Kunze et al. (2002) and Carter and Gregg (2002) use multiple moorings to better estimate average dissipation in the Monterey Canyon stratified turbulent layer, as compared to the single mooring at AXIS, making this a tenuous comparison.

As it is difficult to quantify turbulence, it is hoped that a connection to semidiurnal (and secondary constituent) energy may be useful for models that may not have access to data that can resolve such high-frequency processes, in slope and canyon regions. The multivariate power law fits were found to be $\varepsilon \sim M_2^{0.83 \pm 0.17} + \text{Sub}_{K1}^{0.59 \pm 0.13}$ and $\varepsilon \sim M_2^{1.47 \pm 0.48} + \text{NI}^{0.24 \pm 0.06}$, for SLOPE and AXIS, respectively. This builds on similar results by Klymak et al. (2006) at the Hawaiian Ridge, who found that near the ridge dissipation scaled with semidiurnal energy as $\varepsilon \sim M_2^{1.0 \pm 0.5}$. However, it is not enough to link dissipation to IW and IT driven high-frequency continuum energy, alone, as there are many spatially and temporally variable regional processes that may also contribute, such as large-scale ocean circulation, biogeochemical cycles, weather, and long-term climate (Kunze, 2017). Furthermore, turbulence may be forced intermittently by these phenomena (Klymak et al., 2006), making it difficult to attribute individual contributors over long periods. Use of the observed fits for modelling should be considered with these issues in mind, and improvements could be the subject of further research.

6.5 Near- N spectral shoulder energy

The near- N spectral shoulder is a well known, yet often unresolved feature in ADCP velocity spectra. As early as 1966, Sabinin described a prominent near- N peak that widened with depth, ascribed to IW-buoyancy ringing (Pinkel, 1975), yet beyond the next decade subsequent observations are brief (Kase & Clarke, 1978), and temporally sparse (D'Asaro et al., 2007; Pinkel, 2014; Alford et al., 2016). The long-term, high-frequency sampling in this study allows

for a high Nyquist frequency and low noise floor that fully expose the shoulder, continuing the discussion. Observations indicate that shoulder energy is intermittently depth dependent at SLOPE, and more uniformly so at AXIS, similar to Pinkel's (1975) findings. There is subtle shoulder energy variability at both sites, being generally stronger in the fall, with correlations and power law fits suggesting that shoulder energy is tied to the high-frequency continuum, and therefore dissipation. This agrees with previous theories, arguing that the near- N shoulder is a result of an enhanced cascade of energy from low- to high-frequency turbulent processes due to resonant wave-wave interaction, where energy collects at and above the "resonant buoyancy frequency" (Leder, 2002) - approximately the depth-mean value of N below the buoyancy variable thermocline. In this study, $N_0 = 4.03 \times 10^{-4}$ Hz (averaged around -900 m and varying insubstantially when expanded to the lower thermocline), central to the observed shoulder, and similar to the ~2 cph value of N_0 that defined the spectral shoulder (2 - 5 cph) of Kase and Clarke (1978), who modelled the near- N response with data from the GATE experiment.

However, seasonal forcing of the near- N spectral shoulder is inconsistent between studies. At Barkley Canyon, correlations and power law fits suggest that high-frequency continuum energy is strongly linked to spectral shoulder energy. As these power law fits overlap within uncertainty for both sites (averaging $P_{Sh} \sim \varepsilon^{0.34 \pm 0.08}$), it is possible that this relationship is independent of site topography, likely due to the relatively small spatial scale of near- N motions. Furthermore, as high-frequency continuum energy is strongly suspected to cascade from the semidiurnal constituent (and partially from secondary contributors), the same forcing should apply to the spectral shoulder as the cascade continues. Leder (2002) suggested that solitons forming in the troughs of semidiurnal IT could contribute to near- N energy, but that it is unlikely, and evidence against this theory was provided by D'Asaro et al. (2007) who found no association between shoulder energy and observed solibores. Furthermore, there are no obvious solibores noted in the Barkley Canyon observations. Pinkel (2014) suggested that sub-mesoscale currents could contribute to near- N energy, and both Leder (2002) and Alford et al. (2016) attributed enhanced high-frequency shear to wind-forced NI IW. Forcing by these constituents agrees roughly with the possible secondary contributors to observed high-frequency continuum energy (sub-diurnal at SLOPE, and NI at AXIS), but is conspicuously lacking semidiurnal influence. It is possible that the near- N spectral shoulder does receive energy from the high-frequency continuum, but that turbulent processes are so variable, regionally, that forcing is unique to each study site. Properly quantifying the nature of this enhanced cascade of energy is important for better understanding the effects of turbulence and

1092 mixing, and is left for further study.

1093 7 Summary and conclusions

1094 It was found that there is significant influence from topography on the lo-
1095 cal IW field at both sites. Continental slope and canyon topography guides
1096 flow, with inter-annually consistent, periodic (about a week) up-canyon mean
1097 currents (-700 to -900 m) above a near-bottom down-canyon layer. There is
1098 frequency-dependent focusing of IW energy, generally up to a factor of 10,
1099 130 m above bottom at SLOPE, and up to a factor of 100, 230 m above bot-
1100 tom at AXIS. The near-topography elevated energy has unique seasonality
1101 for individual frequency constituents, and varies little inter-annually. Sub-
1102 diurnal and diurnal flows are presumably sub-inertially trapped along topog-
1103 raphy, and the diurnal band appears to be forced locally (barotropically).
1104 The NI band is attenuated near the slope, yet elevated near the canyon bot-
1105 tom, with intermittent forcing that appears linked to regional wind events,
1106 high-mode propagation, and the seasonal ML depth. Free semidiurnal IT
1107 are focused and reflected near critical topography, and appear to experience
1108 both local and remote (baroclinic) forcing. The high-frequency IW contin-
1109 uum is elevated compared to the open-ocean GM spectrum (up to $7 \times$ GM),
1110 with enhanced dissipation (reaching $10^{-7} \text{ W kg}^{-1}$) and diffusivity (reaching
1111 $10^{-3} \text{ m}^2 \text{ s}^{-1}$) near topography. Dissipation–band-power variability corre-
1112 lations suggest a cascade of energy from the semidiurnal constituent, yielding
1113 inter-annual power law fits of $\varepsilon \sim M_2^{0.42 \pm 0.29}$ at SLOPE, and $\varepsilon \sim M_2^{0.64 \pm 0.30}$
1114 at AXIS. Improved fits accounting for secondary constituents yield power law
1115 relationships of $\varepsilon \sim M_2^{0.83 \pm 0.17} + \text{Sub}_{K1}^{0.59 \pm 0.13}$ at SLOPE, and $\varepsilon \sim M_2^{1.47 \pm 0.48} +$
1116 $\text{NI}^{0.24 \pm 0.06}$ at AXIS. There is evidence of a near- N spectral shoulder which may
1117 collect energy from high-frequency continuum turbulence, possibly an addi-
1118 tional step in the cascade of energy from low- to high-frequency dissipative
1119 processes. The shoulder-dissipation energy variability correlations yield an
1120 average, site-independent power law fit of $P_{Sh} \sim \varepsilon^{0.34 \pm 0.08}$.

1121 Unfortunately, the WKB-stretch scaling applied throughout much of the anal-
1122 ysis is based on deep CTD casts that were made nearby (20 km south of
1123 Barkley Canyon), but away from topography. The stratification profile cap-
1124 tures the surface ML and pycnocline, but does not account for adjustment
1125 near the slope or in the canyon (Figure 9). Hotchkiss and Wunsch (1982)
1126 noted increased stratification near areas of high ‘topographic relief’, such as
1127 the shelf-break and slopes. These highly stratified turbulent layers may more
1128 strongly experience the effects of reflection, scattering, and IT and lee-wave
1129 generation, as well as amplification of IW and IT. To properly account for

1130 the effects of depth-dependent stratification variability, further research would
1131 benefit from site specific climatology data.

1132 Results could be further improved through increased sampling consistency be-
1133 tween instruments (there were maintenance periods and instrument redeploy-
1134 ments during analysis years), additional instrument sites (along the length of
1135 the canyon floor and rim), and additional overlapping comparison years be-
1136 tween sites. Broader temporal coverage could provide insight into long-term
1137 seasonality, while additional spatial coverage would allow for observations of
1138 IW propagation. For NI wind forcing, reanalysis wind data may have provided
1139 better (fewer gaps) temporal coverage for comparison.

1140 Further research is required to: identify forcing for the sub-diurnal range's in-
1141 termittent seasonality and the periodicity of up-canyon mean currents at AXIS;
1142 accurately identify sites of origin for incident baroclinic shelf waves and IT af-
1143 fecting the diurnal and semidiurnal responses; better quantify the downward
1144 propagation of NI IW energy from the ML to the interior; and, improve power
1145 law fits of dissipation and near- N spectral shoulder energy to better model the
1146 cascade of energy from low- to high-frequency turbulent mixing.

1147 Barkley Canyon is a dynamic continental slope and submarine canyon region
1148 with physical processes that are heavily influenced by topography. Continen-
1149 tal slopes and canyons are known as hot-spots for IT generation and IW-
1150 driven turbulence, contributing significantly to regional transport of energy,
1151 shelf productivity, and even large-scale ocean circulation and climate effects.
1152 As regional currents, tides, and wind all contribute to an energetic local IW
1153 field, the Barkley Canyon portion of ONC's NEPTUNE cabled observatory
1154 is an important data network for understanding the effects of topography-IW
1155 interactions on the VICS. Furthermore, results here may be valuable for char-
1156 acterising mixing processes at other slope and canyon sites, and for better
1157 estimating the global IW and IT energy budget. It is hoped that this study
1158 has provided valuable insight leading to further research and collaboration,
1159 and improved knowledge of the importance of shelf-incising canyon regions as
1160 fundamental to both regional and large-scale physical ocean processes.

1161 8 References

- 1162 Alford, M. H. (2001). Internal swell generation: The spatial distribution of
1163 energy flux from the wind to mixed layer near-inertial motions. *Journal
1164 of Physical Oceanography*, 31(8 PART 2), 2359–2368.
- 1165 Alford, M. H., MacKinnon, J. A., Zhao, Z., Pinkel, R., Klymak, J., & Pea-
1166 cock, T. (2007). Internal waves across the Pacific. *Geophysical Research
1167 Letters*, 34(24), 24601.
- 1168 Alford, M. H. (2003). Improved global maps 54-year history of wind-work on
1169 ocean inertial motions. *Geophysical Research Letters*, 30(8), 1424.
- 1170 Alford, M. H. (2020). Revisiting near-inertial wind work: Slab models, relative
1171 stress, and mixed layer deepening. *Journal of Physical Oceanography*,
1172 50(11), 3141–3156.
- 1173 Alford, M. H., Cronin, M. F., & Klymak, J. M. (2012). Annual cycle and
1174 depth penetration of wind-generated near-inertial internal waves at ocean
1175 station papa in the northeast pacific. *Journal of Physical Oceanography*,
1176 42(6), 889–909.
- 1177 Alford, M. H., Mackinnon, J. A., Simmons, H. L., & Nash, J. D. (2016). Near-
1178 Inertial Internal Gravity Waves in the Ocean. *Annual Review of Marine
1179 Science*, 8, 95–123.
- 1180 Alford, M. h., Shcherbina, A. Y., & Gregg, M. C. (2013). Observations of Near-
1181 Inertial Internal Gravity Waves Radiating from a Frontal Jet. *Journal
1182 of Physical Oceanography*, 43(6), 1209–1224.
- 1183 Alford, M. H., & Zhao, Z. (2007). Global patterns of low-mode internal-
1184 wave propagation. Part I: Energy and energy flux. *Journal of Physical
1185 Oceanography*, 37(7), 1829–1848.
- 1186 Allen, S. E., Vindedirinho, C., Thomson, R. E., Foreman, M. G. G., & Mackas,
1187 D. L. (2001). Physical and biological processes over a submarine canyon
1188 during an upwelling event. *Canadian Journal of Fisheries and Aquatic
1189 Sciences*, 58(4), 671–684.
- 1190 Althaus, A. M., Kunze, E., & Sanford, T. B. (2003). Internal tide radiation
1191 from Mendocino escarpment. *Journal of Physical Oceanography*, 33(7),
1192 1510–1527.
- 1193 Anstey, K. (2022). Internal waves at Barkley Canyon. Retrieved from GitHub
1194 website: https://github.com/kurtisanstey/internal_waves_barkley_canyon

- 1195 Arbic, B. K., Richman, J. G., Shriver, J. F., Timko, P. G., Joseph Metzger, E.,
1196 & Wallcraft, A. J. (2012). Global modeling of internal tides within an
1197 eddying ocean general circulation model. *Oceanography*, 25(2), 20–29.
- 1198 Brink, K. H. (1991). Coastal-trapped waves and wind-driven currents over the
1199 continental shelf. *Annual Review of Fluid Mechanics*, 23(1), 389–412.
- 1200 Burrier, D. A. (2019). The Internal Wave Dynamics of Barkley Submarine
1201 Canyon. San Jose State University.
- 1202 Cabrera, F., Ogata, B., Sastri, A. R., Heesemann, M., Mihály, S., Galbraith,
1203 M., & Morley, M. G. (2018). High-frequency observations from a deep-
1204 sea cabled observatory reveal seasonal overwintering of *Neocalanus* spp.
1205 in Barkley Canyon, NE Pacific: Insights into particulate organic carbon
1206 flux. *Progress in Oceanography*, 169, 120–137.
- 1207 Carter, G. S., & Gregg, M. C. (2002). Intense, variable mixing near the head
1208 of Monterey Submarine Canyon. In *Journal of Physical Oceanography*
1209 (Vol. 32).
- 1210 Chauvet, P., Metaxas, A., Hay, A. E., & Matabos, M. (2018). Annual and
1211 seasonal dynamics of deep-sea megafaunal epibenthic communities in
1212 Barkley Canyon (British Columbia, Canada): A response to climatology,
1213 surface productivity and benthic boundary layer variation. *Progress in
1214 Oceanography*, 169, 89–105.
- 1215 Crawford, W. R. (1984). Energy flux and generation of diurnal shelf waves
1216 along Vancouver Island. *J. Phys. Oceanogr.*, 14(10, Oct. 1984), 1600–1607.
- 1217 Crawford, W. R., & Thomson, R. E. (1984). Diurnal-Period Continental Shelf
1218 Waves along Vancouver Island: A Comparison of Observations with The-
1219 retical Models. *Journal of Physical Oceanography*, 14(10), 1629–1646.
- 1220 Cummins, P. F., Masson, D., & Foreman, M. G. G. (2000). Stratification and
1221 mean flow effects on diurnal tidal currents off Vancouver Island. *Journal
1222 of Physical Oceanography*, 30(1), 15–30.
- 1223 Cummins, P. F., & Oey, L. Y. (1997). Simulation of barotropic and baroclinic
1224 tides off northern British Columbia. *Journal of Physical Oceanography*,
1225 27(5), 762–781.
- 1226 D'Asaro, E. A. (1985). The energy flux from the wind to near-inertial motions
1227 in the surface mixed layer. *J. Phys. Oceanogr.*, 15(8, Aug. 1985),
1228 1043–1059.
- 1229 D'Asaro, E. A. (1995). Upper-ocean inertial currents forced by a strong storm.

- 1230 Part III: interaction of inertial currents and mesoscale eddies. *Journal
1231 of Physical Oceanography*, 25(11 Part II), 2953–2958.
- 1232 D'Asaro, E. A., Lien, R. C., & Henyey, F. (2007). High-frequency internal
1233 waves on the Oregon continental shelf. *Journal of Physical Oceanogra-
1234 phy*, 37(7), 1956–1967.
- 1235 Doya, C., Aguzzi, J., Pardo, M., Matabos, M., Company, J. B., Costa, C., ...
1236 Canals, M. (2014). Diel behavioral rhythms in sablefish (*Anoplopoma
1237 fimbria*) and other benthic species, as recorded by the Deep-sea cabled
1238 observatories in Barkley canyon (NEPTUNE-Canada). *Journal of Ma-
1239 rine Systems*, 130, 69–78.
- 1240 Drakopoulos, P. G., & Marsden, R. F. (1993). The internal tide off the west
1241 coast of Vancouver Island. *Journal of Physical Oceanography*, 23(4),
1242 758–775.
- 1243 Flather, R. A. (1988). A numerical model investigation of tides and diurnal-
1244 period continental shelf waves along Vancouver Island. *J. Phys. Oceanogr.*,
1245 18(1, Jan. 1988), 115–139.
- 1246 Garratt, J. R. (1977). Review of Drag Coefficients over Oceans and Continents.
1247 *Monthly Weather Review*, 105(7), 915–929.
- 1248 Garrett, C., & Kunze, E. (2007). Internal tide generation in the deep ocean.
1249 *Annual Review of Fluid Mechanics*, 39, 57–87.
- 1250 Garrett, C. (2005). 2004 Program of Study: Tides Course Lectures Fellows
1251 Project Reports.
- 1252 Gemmrich, J., & Klymak, J. M. (2015). Dissipation of internal wave energy
1253 generated on a critical slope. *Journal of Physical Oceanography*, 45(9),
1254 2221–2238.
- 1255 Gill, A. E. (1984). On the Behavior of Internal Waves in the Wakes of Storms.
1256 *Journal of Physical Oceanography*, 14(7), 1129–1151.
- 1257 Gonella, J. (1972). A rotary-component method for analysing meteorolog-
1258 ical and oceanographic vector time series. In *Deep-Sea Research and
1259 Oceanographic Abstracts* (Vol. 19).
- 1260 Gregg, M. C. (1989). Scaling turbulent dissipation in the thermocline. *Journal
1261 of Geophysical Research*, 94(C7), 9686.
- 1262 Hotchkiss, F. S., & Wunsch, C. (1982). Internal waves in Hudson Canyon with
1263 possible geological implications. *Deep Sea Research Part A, Oceano-*

- 1264 graphic Research Papers, 29(4), 415–442.
- 1265 Jarosz, E., Hallock, Z. R., & Teague, W. J. (2007). Near-inertial currents in the
1266 DeSoto Canyon region. *Continental Shelf Research*, 27(19), 2407–2426.
- 1267 Juniper, S. K., Matabos, M., Mihály, S., Ajayamohan, R. S., Gervais, F., &
1268 Bui, A. O. V. (2013). A year in Barkley Canyon: A time-series observa-
1269 tory study of mid-slope benthos and habitat dynamics using the NEP-
1270 TUNE Canada network. *Deep-Sea Research Part II: Topical Studies in*
1271 *Oceanography*, 92, 114–123.
- 1272 Käse, R. H., & Allyn Clarke, R. (1978). High frequency internal waves in the
1273 upper thermocline during GATE. *Deep-Sea Research*, 25(9), 815–825.
- 1274 Klymak, J. M., Alford, M. H., Pinkel, R., Lien, R. C., Yang, Y. J., & Tang,
1275 T. Y. (2011). The breaking and scattering of the internal tide on a
1276 continental slope. *Journal of Physical Oceanography*, 41(5), 926–945.
- 1277 Klymak, J. M., Moum, J. N., Nash, J. D., Kunze, E., Girton, J. B., Carter,
1278 G. S., ... Gregg, M. C. (2006). An estimate of tidal energy lost to
1279 turbulence at the Hawaiian Ridge. *Journal of Physical Oceanography*,
1280 36(6), 1148–1164.
- 1281 Kundu, P. K., & Cohen, I. (2008). Fluid mechanics. (4th ed.). Academic
1282 Press.
- 1283 Kunze, E. (1985). Near-Inertial Wave Propagation In Geostrophic Shear.
1284 *Journal of Physical Oceanography*, 15(5), 544–565.
- 1285 Kunze, E. (2017). Internal-wave-driven mixing: Global geography and bud-
1286 gets. *Journal of Physical Oceanography*, 47(6), 1325–1345.
- 1287 Kunze, E., Mackay, C., Mcphee-Shaw, E. E., Morrice, K., Girton, J. B., &
1288 Terker, S. R. (2012). Turbulent mixing and exchange with interior wa-
1289 ters on sloping boundaries. *Journal of Physical Oceanography*, 42(6),
1290 910–927.
- 1291 Kunze, E., Rosenfeld, L. K., Carter, G. S., & Gregg, M. C. (2002). Internal
1292 waves in Monterey Submarine Canyon. *Journal of Physical Oceanogra-
1293 phy*, 32(6), 1890–1913.
- 1294 Lamb, K. G. (2014). Internal wave breaking and dissipation mechanisms
1295 on the continental slope/shelf. *Annual Review of Fluid Mechanics*, 46,
1296 231–254.
- 1297 Lavelle, J. W., & Cannon, G. A. (2001). On subinertial oscillations trapped

- 1298 by the Juan de Fuca Ridge, northeast Pacific. In *Journal of Geophysical*
1299 *Research: Oceans* (Vol. 106).
- 1300 Leder, N. (2002). Wind-induced internal wave dynamics near the Adriatic
1301 shelf break. In *Continental Shelf Research* (Vol. 22).
- 1302 Levine, M. D. (2002). A modification of the Garrett-Munk internal wave
1303 spectrum. *Journal of Physical Oceanography*, 32(11), 3166–3181.
- 1304 Li, M., Myers, P. G., & Freeland, H. (2005). An examination of historical
1305 mixed layer depths along Line P in the Gulf of Alaska. *Geophysical*
1306 *Research Letters*, 32(5), 1–4.
- 1307 Martini, K. I., Alford, M. H., Kunze, E., Kelly, S. M., & Nash, J. D. (2011).
1308 Observations of internal tides on the oregon continental slope. *Journal*
1309 *of Physical Oceanography*, 41(9), 1772–1794.
- 1310 Martini, K. I., Alford, M. H., Kunze, E., Kelly, S. M., & Nash, J. D. (2013).
1311 Internal bores and breaking internal tides on the Oregon continental
1312 slope. *Journal of Physical Oceanography*, 43(1), 120–139.
- 1313 Mihaly, S. F., Thomson, R. E., & Rabinovich, A. B. (1998). Evidence for
1314 nonlinear interaction between internal waves of inertial and semidiurnal
1315 frequency. *Geophysical Research Letters*, 25(8), 1205–1208.
- 1316 Morozov, E. G. (2018). Semidiurnal Internal Wave Global Field; Global Esti-
1317 mates of Internal Tide Energy. In *Oceanic Internal Tides: Observations,*
1318 *Analysis and Modeling* (pp. 263–291).
- 1319 Munk, W., & Garrett, C. (1979). Internal Waves and Small-Scale Processes.
1320 In C. Wunsch (Ed.), *Evolution of Physical Oceanography*.
- 1321 Munk, W., & Wunsch, C. (1998). Abyssal recipes II: Energetics of tidal and
1322 wind mixing. *Deep-Sea Research Part I: Oceanographic Research Papers*,
1323 45(12), 1977–2010.
- 1324 Nash, J. D., Kunze, E., Toole, J. M., & Schmitt, R. W. (2004). Internal tide
1325 reflection and turbulent mixing on the continental slope. In *Journal of*
1326 *Physical Oceanography* (Vol. 34).
- 1327 Petruncio, E. T., Rosenfeld, L. K., & Paduan, J. D. (1998). Observations of
1328 the internal tide in Monterey Canyon. *Journal of Physical Oceanography*,
1329 28(10), 1873–1903.
- 1330 Pinkel, R. (1975). Upper ocean internal wave observations from Flip. *Journal*
1331 *of Geophysical Research*, 80(27), 3892–3910.

- 1332 Pinkel, R. (2014). Vortical and internal wave shear and strain. *Journal of*
1333 *Physical Oceanography*, 44(8), 2070–2092.
- 1334 Polzin, K. L., & Lvov, Y. V. (2011). Toward regional characterizations of the
1335 oceanic internal wavefield. *Reviews of Geophysics*, 49(4), 4003.
- 1336 Polzin, K. L., Toole, J. M., Ledwell, J. R., & Schmitt, R. W. (1997). Spatial
1337 variability of turbulent mixing in the abyssal ocean. *Science*, 276(5309),
1338 93–96.
- 1339 Polzin, K. (2004). A heuristic description of internal wave dynamics. *Journal*
1340 *of Physical Oceanography*, 34(1), 214–230.
- 1341 Robertson, R., Dong, J., & Hartlipp, P. (2017). Diurnal Critical Latitude and
1342 the Latitude Dependence of Internal Tides, Internal Waves, and Mixing
1343 Based on Barcoo Seamount. *Journal of Geophysical Research: Oceans*,
1344 122(10), 7838–7866.
- 1345 Rudnick, D. L., Gopalakrishnan, G., & Cornuelle, B. D. (2015). Cyclonic eddies
1346 in the Gulf of Mexico: Observations by underwater gliders and sim-
1347 ulations by numerical model. *Journal of Physical Oceanography*, 45(1),
1348 313–326.
- 1349 Sun, H., & Kunze, E. (1999). Internal wave-wave interactions. Part I: The role
1350 of internal wave vertical divergence. *Journal of Physical Oceanography*,
1351 29(11), 2886–2904.
- 1352 Terker, S. R., Girton, J. B., Kunze, E., Klymak, J. M., & Pinkel, R. (2014).
1353 Observations of the internal tide on the California continental margin
1354 near Monterey Bay. *Continental Shelf Research*, 82, 60–71.
- 1355 Thomson, R. E., & Crawford, W. R. (1982). The Generation of Diurnal Period
1356 Shelf Waves by Tidal Currents in: *Journal of Physical Oceanography*
1357 Volume 12 Issue 7 (1982). *Journal of Physical Oceanography*, 12(7).
- 1358 Thomson, R. E., & Emery, W. J. (2014). Data Analysis Methods in Physical
1359 Oceanography: Third Edition. In *Data Analysis Methods in Physical*
1360 *Oceanography: Third Edition (Third)*.
- 1361 Thomson, R. E., & Fine, I. V. (2003). Estimating mixed layer depth from
1362 oceanic profile data. *Journal of Atmospheric and Oceanic Technology*,
1363 20(2), 319–329.
- 1364 Thomson, R. E., & Krassovski, M. V. (2015). Remote alongshore winds
1365 drive variability of the California Undercurrent off the British Columbia-
1366 Washington coast. *Journal of Geophysical Research: Oceans*, 120(12),

- 1367 8151–8176.
- 1368 Thomson, R. E., Roth, S. E., & Dymond, J. (1990). Near-inertial motions
1369 over a mid-ocean ridge: Effects of topography and hydrothermal plumes.
1370 *Journal of Geophysical Research*, 95(C5), 7261.
- 1371 Thorpe, S. A. (2001). On the Reflection of Internal Wave Groups from Sloping
1372 Topography. *Journal of Physical Oceanography*, 31(10), 3121–3126.
- 1373 Voelker, G. S., Olbers, D., Walter, M., Mertens, C., & Myers, P. G. (2020).
1374 Estimates of wind power and radiative near-inertial internal wave flux:
1375 The hybrid slab model and its application to the North Atlantic. *Ocean
1376 Dynamics*, 70(11), 1357–1376.
- 1377 Waterhouse, A. F., Mackinnon, J. A., Musgravea, R. C., Kelly, S. M., Pick-
1378 ering, A., & Nash, J. (2017). Internal tide convergence and mixing in a
1379 submarine canyon. *Journal of Physical Oceanography*, 47(2), 303–322.
- 1380 Xie, X., & Chen, D. (2021). Near-surface reflection and nonlinear effects
1381 of low-mode internal tides on a continental slope. *Journal of Physical
1382 Oceanography*, 51(4), 1037–1051.
- 1383 Xu, J. P., & Noble, M. A. (2009). Currents in monterey submarine canyon.
1384 *Journal of Geophysical Research: Oceans*, 114(3), 3004.
- 1385 Zervakis, V., & Levine, M. D. (1995). Near-inertial energy propagation from
1386 the mixed layer: theoretical considerations. *Journal of Physical Oceanog-
1387 raphy*, 25(11 Part II), 2872–2889.
- 1388 Zhai, X., Greatbatch, R. J., & Zhao, J. (2005). Enhanced vertical propagation
1389 of storm-induced near-inertial energy in an eddying ocean channel model.
1390 *Geophysical Research Letters*, 32(18), 1–4.
- 1391 Zhao, Z., Alford, M. H., Girton, J. B., Rainville, L., & Simmons, H. L. (2016).
1392 Global observations of open-ocean mode-1 M2 internal tides. *Journal of
1393 Physical Oceanography*, 46(6), 1657–1684.
- 1394 Zhao, Z. (2017). Propagation of the Semidiurnal Internal Tide: Phase Velocity
1395 Versus Group Velocity. *Geophysical Research Letters*, 44(23), 11942–
1396 11950.
- 1397 Zheng, J., Tian, J., & Liang, H. (2017). Observation of near-inertial internal
1398 waves on the continental slope in the northwestern South China Sea.
1399 *Journal of Ocean University of China*, 16(2), 184–190.

1400 **A Appendix: Supplemental plots**

1401 **A.1 Wind comparisons**

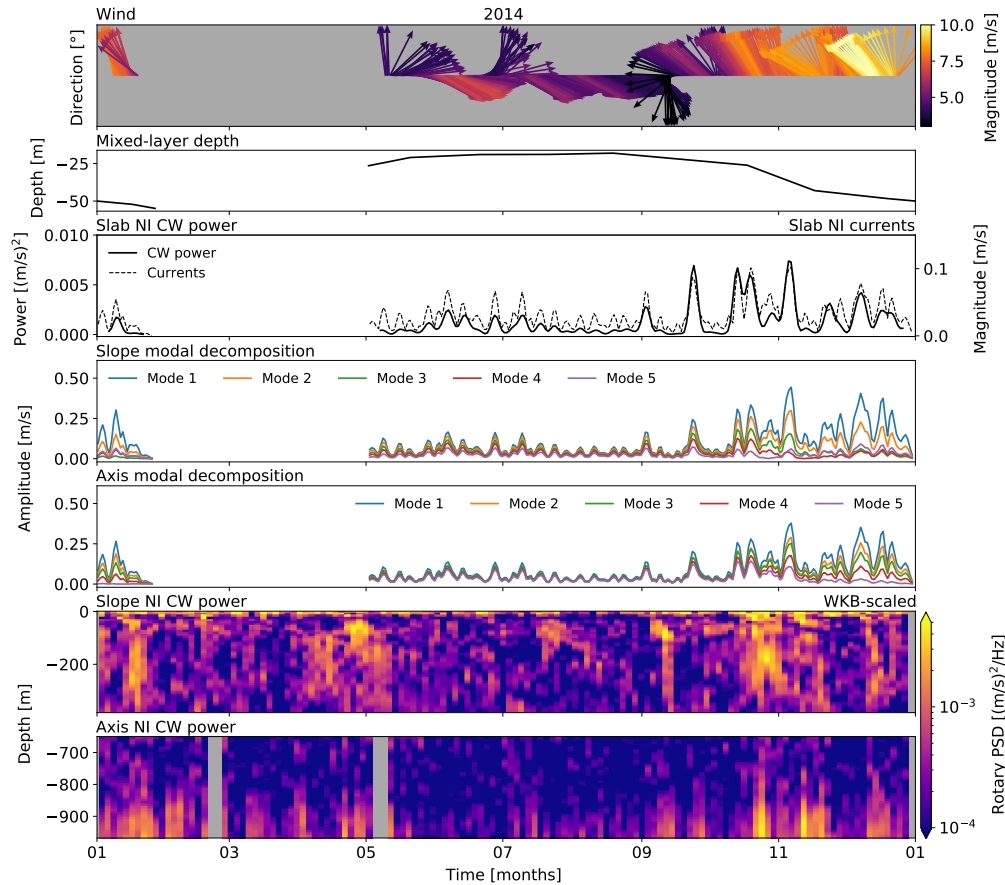


Figure 32. NI forcing analysis for 2014. From top to bottom: wind direction and amplitude; monthly-averaged ML depth for Line P station 3 as determined by Li et al. (2005); slab model NI CW power and NI currents; seasonal mode amplitudes for SLOPE and AXIS; and, band-integrated NI CW power at SLOPE and AXIS. There appears to be a complex relationship between the wind, ML, slab currents, and mode amplitudes in driving the NI observations, with the most obvious effects in the fall.

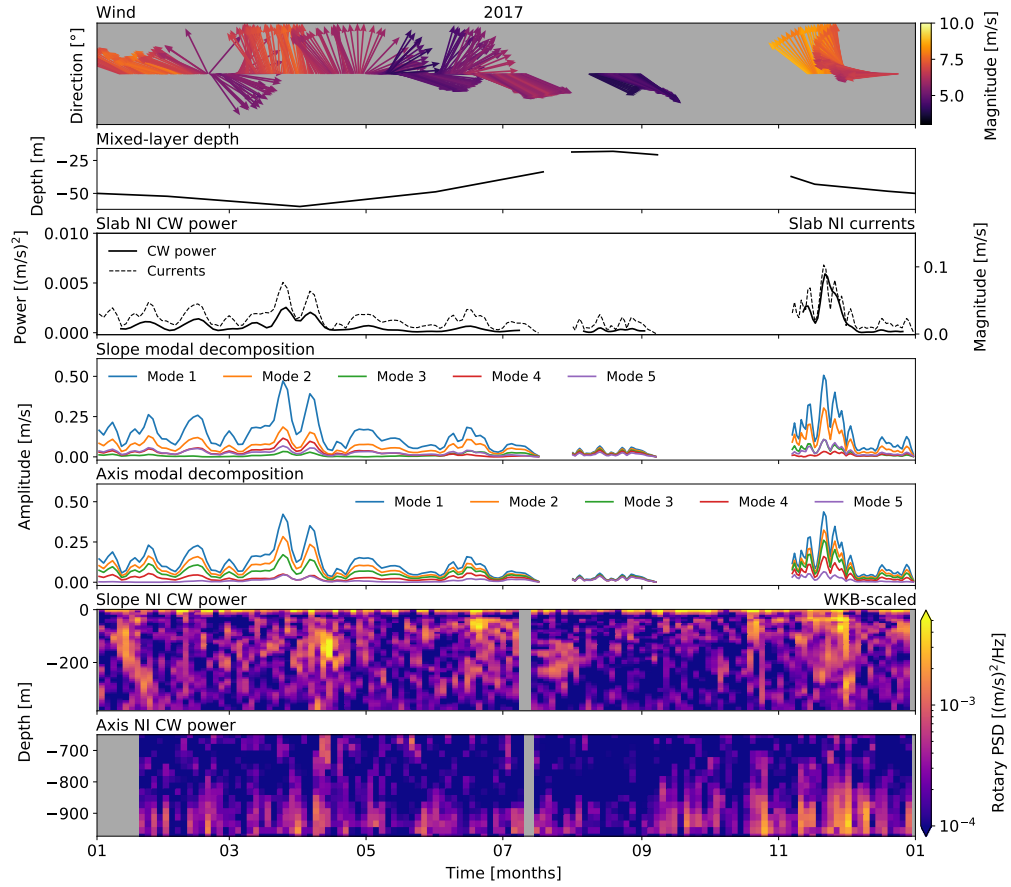


Figure 33. NI forcing analysis for 2017. From top to bottom: wind direction and amplitude; monthly-averaged ML depth for Line P station 3 as determined by Li et al. (2005); slab model NI CW power and NI currents; seasonal mode amplitudes for SLOPE and AXIS; and, band-integrated NI CW power at SLOPE and AXIS. There appears to be a complex relationship between the wind, ML, slab currents, and mode amplitudes in driving the NI observations, with the most obvious effects in the fall.

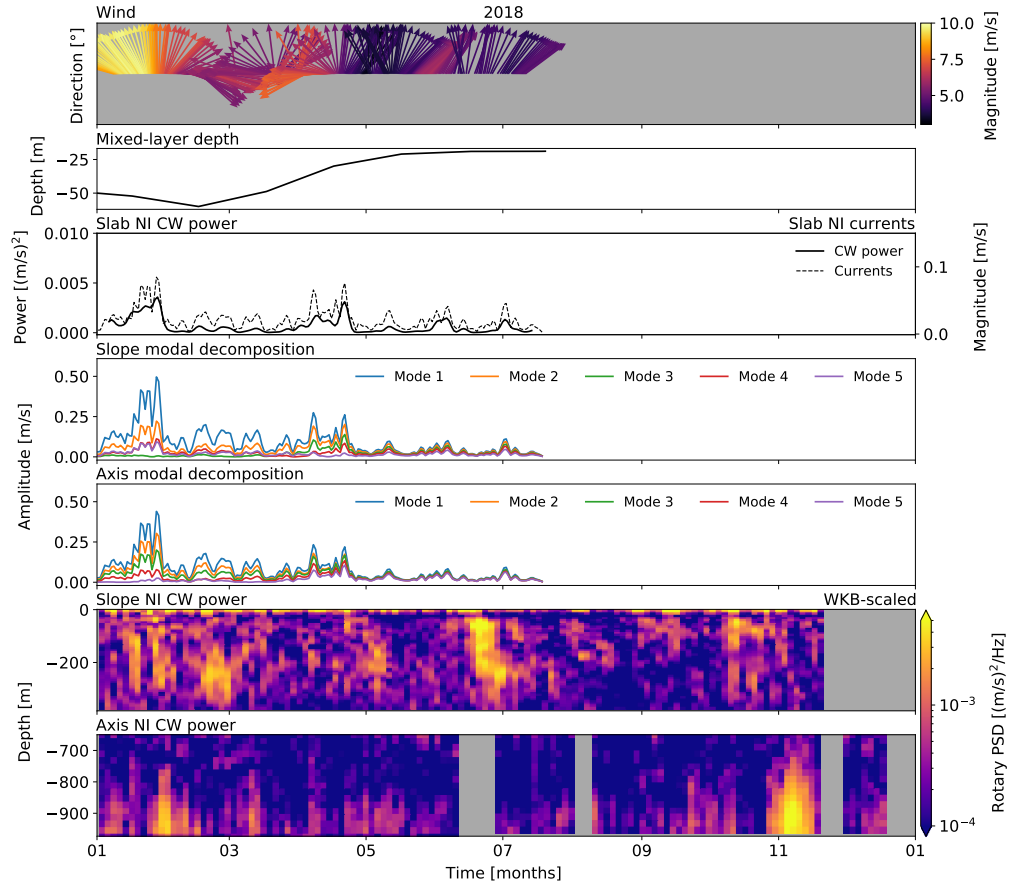


Figure 34. NI forcing analysis for 2018. From top to bottom: wind direction and amplitude; monthly-averaged ML depth for Line P station 3 as determined by Li et al. (2005); slab model NI CW power and NI currents; seasonal mode amplitudes for SLOPE and AXIS; and, band-integrated NI CW power at SLOPE and AXIS. There appears to be a complex relationship between the wind, ML, slab currents, and mode amplitudes in driving the NI observations, with the most obvious effects in the fall.